

Mieap forms membraneless organelles to compartmentalize and facilitate cardiolipin metabolism

Naoki Ikari

National Cancer Center Research Institute

Katsuko Honjo

National Cancer Center Research Institute

Yoko Sagami

National Cancer Center Research Institute

Yasuyuki Nakamura

National Cancer Center Research Institute

Hirofumi Arakawa (✉ harakawa@ncc.go.jp)

National Cancer Center Research Institute <https://orcid.org/0000-0001-6077-0638>

Article

Keywords: Mieap, intrinsically disordered regions, mitochondria, cardiolipin, metabolism, membrane-less organelles, phase separation, liquid droplets, spata18

Posted Date: June 22nd, 2022

DOI: <https://doi.org/10.21203/rs.3.rs-713092/v2>

License:  This work is licensed under a Creative Commons Attribution 4.0 International License.

[Read Full License](#)

Abstract

Biomolecular condensates function as membraneless organelles that compartmentalize and facilitate efficient biological reactions. They are formed by proteins with intrinsically disordered regions (IDRs) via liquid–liquid phase separation. Mieap/SPATA18, a p53-inducible protein, participates in suppression of colorectal tumors by promoting mitochondrial quality control. However, the regulatory mechanism involved remains unclear. Here, we report that Mieap is an IDR-containing protein that drives formation of biomolecular condensates in mitochondria. Mieap biomolecular condensates specifically phase separate the mitochondrial phospholipid, cardiolipin. Lipidomic analysis of cardiolipin suggests that Mieap promotes enzymatic reactions involved in cardiolipin metabolism, including biosynthesis and remodeling. Accordingly, four cardiolipin biosynthetic enzymes, TMM41, PGS1, PTPMT1, and CRLS1, and two remodeling enzymes, PLA2G6 and TAZ, are phase-separated by Mieap biomolecular condensates. Mieap-deficient mice exhibit altered crista structure in mitochondria of various tissues, including brown fat, and tend to become obese. These results suggest that Mieap drives formation of membraneless organelles to compartmentalize and promote cardiolipin metabolism at the inner mitochondrial membrane, thus potentially contributing to mitochondrial quality control.

Introduction

Biomolecular condensates (BCs) in cells are also known as liquid droplets because of their liquid-like nature. BCs are composed of proteins, nucleic acids, and other macromolecular components¹⁻³, and they are formed by proteins with intrinsically disordered regions (IDRs) via liquid–liquid phase separation (LLPS). Importantly, BCs function as membraneless organelles (MLOs) that compartmentalize and facilitate cellular biological reactions. BCs are not surrounded by lipid bilayers, which enables facile exchange of reactants and products with their surroundings, expediting biological reactions in cells. Furthermore, theoretically, BCs are able to appear and disappear within a cell in response to cellular stress and/or subcellular circumstances, exhibiting spatiotemporally dynamic properties. On the basis of these features, the concept of MLOs is fundamentally different from the long-standing concept of membrane-bound organelles, such as nuclei, lysosomes, mitochondria, and endoplasmic reticulum, stable structures that segregate biomolecules and biological reactions using lipid bilayer membranes. Multiple MLOs may exist within a cell, possibly regulating cellular biological reactions and activities, including transcriptional regulation⁴, signal transduction^{5,6}, immunity⁷, centrosome activity⁸, and mitosis⁹. This list is rapidly growing.

Metabolic reactions are believed to be highly organized through spatiotemporal clustering and compartmentalization of sequential enzymes and substrates/intermediates at subcellular sites, which maximizes efficiency of linked reactions¹⁰. Without this mechanism, small, toxic intermediates, derived from metabolic reactions, rapidly diffuse throughout the cytoplasm. Thus, the concept of subcellular compartmentalization of metabolic reactions has been anticipated for a long time. It was initially

conceived as a “metabolon,” a structural-functional complex of sequential metabolic enzymes and substrates/intermediates¹¹. The “metabolon” concept predicted that sequential enzymes and cellular structural elements form a supramolecular complex for metabolic reactions. In fact, many studies have demonstrated that enzyme clustering *in vivo* may facilitate sequential enzymatic metabolic reactions¹²⁻¹⁵. Among them, “purinosomes” involved in purine metabolism, were the first demonstration of enzyme clustering, revealed by live-cell imaging of six sequential enzymes for *de novo* purine synthesis¹⁶. Although MLOs that compartmentalize and expedite metabolic reactions in cells could address regulatory mechanisms for sequential metabolic reactions, there has been no clear evidence for metabolic MLOs until now.

So far, two studies demonstrated the roles and regulatory mechanisms of MLOs (BCs) in enzymatic reactions. Kim and Tsang et al. reported that modifications of IDRs of scaffold proteins control architecture and enzymatic activity within MLOs¹⁷. In terms of MLOs involved in RNA processing, utilizing the IDRs of FMRP and CAPRIN1, they demonstrated that RNA adenylation and translation are inversely controlled by phosphorylation patterns of the IDRs, which change condensate architecture and enzymatic activity. Peeples and Rosen reported that enzymatic reactions in condensates are accelerated by both mass action and change in substrate K_M ¹⁸. Utilizing a synthetic system where the SUMOylation enzyme cascade is recruited into engineered condensates, they demonstrated that reaction rates can be increased up to 36-fold in condensates compared to the surrounding bulk, and that condensates can modulate reaction rates by not only concentrating enzymes and substrates, but also by physically organizing them. These results strongly suggest the importance of MLOs in regulation of sequential enzymatic reactions in metabolism.

Cardiolipin (CL) is an important phospholipid for the following reasons. [1] It is a phospholipid dimer, with two phosphate residues and four fatty acyl chains¹⁹. [2] Because of this unique structure, it forms a cone shape, contributing to curvature of the lipid membrane and to maintenance of mitochondrial cristae²⁰. [3] CL is the only phospholipid that is specific to mitochondria and is mainly located at the inner mitochondrial membrane and contact sites²⁰. [4] CL interacts with many mitochondrial membrane proteins, including electron transport chain complexes involved in oxidative phosphorylation, and the ADP/ATP carrier. Interaction with CL promotes activity of these proteins²⁰. [5] CL stabilizes the structural assembly and activity of respiratory super-complexes at the inner mitochondrial membrane²¹. [6] It interacts with cytochrome *c* at the outer surface of the inner mitochondrial membrane, which supports cellular viability by maintaining stable respiratory ATP production and inducing apoptosis, respectively²¹. Therefore, control of CL quality and quantity appears to be important for various mitochondrial functions.

CL metabolic reactions comprise two processes, CL biosynthesis and remodeling. CL metabolic enzymes are characterized and studied in yeast cells, and human orthologs of yeast enzymes have been reported²². In brief, phosphatidic acid (PA) is synthesized in the endoplasmic reticulum and subsequently transported by PRELI (yeast Ups1) via the outer mitochondrial membrane to the inner mitochondrial membrane, as the substrate of CL metabolism^{22,23}. In CL biosynthesis, PA is converted to nascent CL on

the matrix face of the inner mitochondrial membrane through sequential enzymatic reactions that produce three intermediates, CDP-diacylglycerol (CDP-DG), phosphatidylglycerophosphate (PGP), and phosphatidylglycerol (PG). These reactions are catalyzed by a series of four enzymes, TAMM41 (yeast Tam41), PGS1 (yeast Pgs1), PTPMT1 (yeast Gep4), and CRLS1 (yeast Crd1) (20,22). The final step of CL metabolic reactions is remodeling of nascent CL to mature CL, which is catalyzed by PLA2G6/iPLA2 β (yeast Cld1) and TAZ (yeast Taz1)^{22,24}. These cascading enzymatic reactions are thought to be continuously executed at the inner mitochondrial membrane. However, how these enzymatic reactions can be continuous and/or how CL metabolic reactions are regulated remain unknown.

Altered CL metabolism and/or deterioration of CL quality and quantity due to CL metabolic enzyme deficiency causes various mitochondrial dysfunctions in eukaryotes ranging from yeast to mammals^{22,25}. Specifically, Barth syndrome is a human disease caused by mutations in the TAZ gene encoding tafazzin, the enzyme responsible for CL remodeling²⁶. Clinical symptoms of Barth syndrome patients include cardiomyopathy, skeletal muscle weakness, neutropenia, and growth retardation. Barth syndrome models, including lymphoblasts and induced pluripotent stem cells derived from patients, exhibit abnormal crista structures, decreased respiration activity, and increased reactive oxygen species (ROS) generation in mitochondria^{27,28}. This implies that substantial regulation of CL metabolic reactions is required to maintain mitochondrial functions and to prevent diseases. However, the regulatory mechanism for CL metabolic reactions is unknown.

Mitochondria-eating protein (Mieap, also denominated SPATA18) was originally identified as a p53-inducible protein. Its mRNA expression is directly regulated by the tumor suppressor, p53, in response to various cellular stresses, including DNA damage²⁹. Mieap expression is lost in nearly 50% of human cancer cell lines due to promoter methylation. Mieap-deficient LS174T colorectal cancer cells generate higher levels of mitochondrial ROS and synthesize less ATP. Mitochondrial ROS in Mieap-deficient colorectal cancer and gastric cancer cells enhances migration and invasiveness of cancer cells under hypoxic conditions^{30,31}. Mieap deficiency promotes intestinal tumors in *Apc^{Min/+}* mice³². Tumors in Mieap-deficient *Apc^{Min/+}* mice reveal abnormal mitochondrial morphology, such as large size, round shape, and disordered cristae. Mieap expression is defective in thyroid oncocytic cell tumors, which accumulate abnormal mitochondria in tumor cells³³. Mieap-regulated mitochondrial quality control is inactivated in tumor tissues of nearly 70% of colorectal cancer and 25% of breast cancer patients^{30,34}. These observations suggest that Mieap suppresses tumors via mitochondrial quality control. However, the mechanism underlying regulation of mitochondrial quality control by Mieap remains unclear.

Here, we report that Mieap is an IDR-containing protein that drives BC formation in mitochondria. Mieap BCs phase separate the mitochondrial phospholipid, CL. The present findings suggest that Mieap BCs function as MLOs that compartmentalize and promote CL synthesis and remodeling reactions at the inner mitochondrial membrane, leading to stabilization of oxidative phosphorylation and suppression of mitochondrial ROS generation. Thus, we suggest that the Mieap-CL axis is the regulatory mechanism for efficient CL metabolic reactions and/or CL quality and quantity control, forming MLOs that govern

mitochondrial quality control by regulating CL synthesis and remodeling. Dysregulation of this pathway leads to mitochondrial dysfunction due to CL alterations, causing a variety of diseases and/or pathologies, including cancer, obesity, and infertility.

Results

Mieap forms biomolecular condensates in mitochondria

Mieap has been reported to form vacuole-like structures, designated as Mieap-induced vacuoles (MIVs), which were thought to directly assimilate mitochondria³⁵ in a non-canonical type of mitophagy. To examine MIV formation and “non-canonical mitophagy” in live cells, we constructed a recombinant adenovirus to express EGFP-tagged Mieap and observed cells expressing EGFP-Mieap using confocal live-cell imaging. Multiple spherical green signals (EGFP-Mieap) appeared around the red mitochondrial signals (MitoTracker Red) (Supplementary Fig. 1a and Movie 1). These oval green signals fused, enlarged, and eventually coalesced into a few large, spherical structures. In contrast, red mitochondrial signal intensity decreased during this process. These results were consistent with our previous interpretation of non-canonical mitophagy; however, they also indicated that the structures formed by EGFP-Mieap are not the ring-shaped formations, previously reported using immunofluorescence (IF)³⁵.

Thus, we repeated the IF experiment on structures comprising EGFP-Mieap. EGFP-Mieap reproducibly formed green condensates, while antibodies (anti-Mieap antibody and anti-GFP antibody) produced ring-shaped staining around the green condensates (Supplementary Fig. 1b). Thus, we suspected that antibodies are unable to permeabilize EGFP-Mieap condensates.

We performed additional IF using anti-FLAG antibody for the MIV structures, which comprise N-FLAG-Mieap (N-terminal FLAG-tagged Mieap protein) and C-FLAG-Mieap (C-terminal FLAG-tagged Mieap protein). Ring-shaped staining was observed with N-FLAG-Mieap, but not C-FLAG-Mieap (Supplementary Fig. 1c), suggesting that Mieap may be positioned with its N-terminal domain facing outward at the surface of the condensates.

Using transmission electron microscopy (TEM), MIV structures appeared to consist of two phases: a dominant electron-dense phase that stained strongly with OsO₄, and an OsO₄-negative, electron-lucent minor phase (Supplementary Fig. 1d). In immunoelectron microscopy (IEM) analysis with anti-Mieap antibody, gold colloid staining indicated that Mieap protein was distributed over the major electron-dense phase (Supplementary Fig. 1e). Thus, both fluorescent tagging and antigen-antibody reactions confirmed that Mieap forms protein condensates, a process fundamentally distinct from “mitophagy.” Mieap condensates exhibited spherical or oval shapes, fusion, and multi-phase structure consisting of two phases: a Mieap-containing phase and a Mieap-depleted phase (Supplementary Fig. 1d, e, and Movie 2). These characteristics, and their propensity to fuse, are not contradictory to a notion that Mieap condensates have liquid-like properties, suggesting that these structures are droplets³. Therefore, we designate Mieap-induced structures as Mieap BCs (Mi-BCs).

To clarify the spatial relationship between Mi-BCs and mitochondria, we performed live-cell imaging using cells co-expressing EGFP-Mieap and an outer mitochondrial membrane marker, mApple-TOMM20 (Supplementary Fig. 1f). In order to thoroughly evaluate the relationship between Mi-BCs and mitochondria, we captured images of nascent Mi-BCs before their enlargement. mApple-TOMM20 entirely surrounded small Mi-BCs, suggesting that Mieap forms condensates in mitochondria (Fig. 1 a – c, and Supplementary Movie 3). Furthermore, our imaging analysis indicated that even enlarged Mi-BCs may exist inside mitochondria (Fig. 1d).

Recently, a study reported that mitochondrial nucleoids exhibit droplet-like features³⁶. Therefore, Mi-BCs are likely the second example of mitochondrial droplets. Considering the efficiency and precision of imaging analyses, we examined the relatively enlarged Mi-BCs in the following experiments.

Mieap is an IDR-containing protein with potential to drive LLPS

We performed *in silico* sequence analyses. Mieap orthologs were found in eukaryotes, but not in bacteria, archaea, or viruses (Fig. 2a)³⁷. Hence, the Mieap function evolved in eukaryotes. Moreover, among eukaryotes, Mieap orthologs were found in metazoans, but not in fungi (Fig. 2a), suggesting that Mieap is beneficial to multicellular organisms.

Using prediction tools³⁸⁻⁴⁰, we determined that Mieap has four IDRs occurring around two coiled-coil (CC) domains (amino acids 92–311: IDR1 to IDR3) and in the C-terminus (amino acids 499–538: IDR4) (Fig. 2b – e), suggesting that Mieap can potentially drive LLPS³.

All four IDRs are enriched in arginine (R, positively charged) and serine (S, uncharged polar) (Fig. 2b). Additionally, IDR1 is enriched in aspartic acid (D, negatively charged), and IDR2 is enriched in glutamic acid (E, negatively charged). D and E were mixed with positively charged residues in IDR1 and IDR2, respectively. In contrast, IDR3 and IDR4 formed clusters of positively charged residues, characterized by repeats of R and S (Fig. 2b – e)⁴¹.

Although amino acid sequences of the IDRs are evolutionarily divergent compared to the structured regions, the distribution of IDRs and clusters of positively charged residues in IDR3 and IDR4 are evolutionarily conserved (Fig. 2c, e, and Supplementary Fig. 2)⁴¹. In addition, there is an evolutionarily conserved hydrophobic character in the Mieap sequence as a whole, the N-terminal half being hydrophilic and the C-terminal half being hydrophobic (Fig. 2d, e, and Supplementary Fig. 2)⁴². This implies that Mieap protein may act as a cellular biosurfactant.

These molecular features in Mieap IDRs are consistent with the concept of the “evolutionary signature” that Zarin et al. previously proposed⁴³. They found that although the amino acid sequences of IDRs are poorly conserved in alignment, most disordered regions contain multiple molecular features that are

preserved as an “evolutionary signature”, which can be used to predict IDRs from their amino acid sequences in yeast.

Material state and dynamics of Mi-BCs are determined by specific regions of Mieap

To map sites responsible for the physical state and dynamics of Mi-BCs, using a confocal microscope, we examined cells expressing EGFP-Mieap WT (WT) and three deletion-mutant forms, EGFP-Mieap Δ CC, Δ 275, and Δ 496 (Δ CC, Δ 275, and Δ 496) (Fig. 3a).

All deletion mutants formed condensates, exhibiting distinctive morphologies (Fig. 3b and Supplementary Movie 4). WT formed spherical or oval condensates that assemble near the nucleus and reveal multi-phase structures. In contrast, Δ CC formed lobular condensates near the nucleus, which reveal the single-phase structures. Δ 275 formed spherical condensates without the Mieap-depleted phase, which are distributed throughout the cytoplasm. Δ 496 formed spherical, multi-phase condensates, which are similar to, but smaller and more numerous than WT condensates.

We further examined the relationship between localization of each mutant condensate and mitochondria by performing live-cell imaging of mutants using MitoTracker Red. WT, Δ CC, and Δ 496 condensates appeared in mitochondria, whereas Δ 275 condensates were detected in the cytoplasm away from mitochondria (Fig. 3c and Supplementary Movie 4).

These results suggest that the N-terminal region, containing IDRs (IDR1–3) and spreading over the CC domains, endows Mi-BCs with liquid-like properties. The structured region allows Mi-BCs to reside in mitochondria, and the C-terminal region, containing IDR4, endows Mi-BCs with the capacity to coalesce.

To investigate protein dynamics in Mi-BCs, we performed fluorescence recovery after photobleaching (FRAP) studies for WT, Δ CC, Δ 275, and Δ 496 condensates. During observations up to 60 s after spot-bleaching, with the bleaching depth being $82.2 \pm 8.1\%$, fluorescence intensity of WT, Δ CC, Δ 275, and Δ 496 condensates recovered to $9.9 \pm 4.0\%$, $4.0 \pm 1.0\%$, $94.3 \pm 4.0\%$, and $17.8 \pm 3.1\%$ of their initial values, respectively (Fig. 3d and Supplementary Fig. 3a). Fluorescence recovery of the Δ 275 condensates almost achieved their initial value within the 60-s observation period, indicating the most fluid state.

When we performed less intense laser exposure, which reduced the bleaching depth to $21.2 \pm 4.4\%$, fluorescence recovery increased 60 s after spot-bleaching (WT, $50.4 \pm 8.8\%$; Δ CC, $32.6 \pm 8.8\%$; Δ 275, $94.9 \pm 13.7\%$; Δ 496, $61.5 \pm 10.1\%$) (Supplementary Fig. 3b). The fluorescence recovery rate increased when the number of bleached molecules was small, suggesting that availability may be a rate-limiting factor.

We further examined slow fluorescence recovery up to 15 min. WT and Δ 496 condensates showed continuous fluorescence recovery, which reached $80.4 \pm 10.2\%$ and $94.0 \pm 9.5\%$ of the initial value within 15 min, respectively (Fig. 3e). In contrast, Δ CC condensates reached equilibrium at $37.4 \pm 6.3\%$ of their initial value within 15 min (Fig. 3e). These data suggested that WT condensates, as well as Δ 496 condensates,

consist mainly of mobile materials, but protein availability from their surroundings is limited. Therefore, FRAP analysis data suggested that Mi-BCs exist in mitochondria.

Mieap may phase-separate mitochondrial CL and CL-binding proteins

To identify molecules targeted for phase separation by Mi-BCs, we screened available fluorescence-tagged mitochondrial proteins and mitochondrial fluorescence probes using confocal live-cell imaging. EGFP-BNIP3, EGFP-NIX, AcGFP1-Mito, DsRed2-Mito, and SYBR Green I (a probe for mitochondrial DNA) were localized at mitochondria, but none of them were incorporated into Mi-BCs (Fig. 4a – e, and Supplementary Fig. 4a, b, and Movie 5).

However, 10-N-nonyl acridine orange (NAO) and EGFP-cytochrome *c* were specifically incorporated into Mi-BCs (Fig. 4f, g and Supplementary Fig. 4c and Movie 6). NAO targets CL⁴⁴, and cytochrome *c* is a CL-binding protein²¹. As described above, positively charged residues are enriched in Mieap IDRs (Fig. 2b – e). CL carries a net negative charge⁴⁵. Sequence data reveal the amphiphilicity of Mieap (Fig. 2d – e), and Mi-BCs consist of an electron-dense phase that is positive for OsO₄⁴⁶, according to TEM analysis (Supplementary Fig. 1d), suggesting that Mi-BCs may contain unsaturated lipids. This speculation was further supported by Nile-Red staining (Supplementary Fig. 5a, b). Therefore, we suspected that CL is a bona-fide target for phase separation by Mi-BCs.

CL forms complexes with >60 mitochondrial proteins, such as cytochrome *c*, ATP synthase, and the prohibitin complex⁴⁷. Among them, ATP5F1B, which is a subunit of the ATP synthase complex, and PHB2 were previously listed as candidates for “Mieap-binding” proteins in our Mieap-interactome data⁴⁸. This prompted us to investigate whether additional CL-binding/related proteins (ATP5F1B and PHB2) are phase separated by Mi-BCs.

EGFP-ATP5F1B and EGFP-PHB2 localized at mitochondria and then became distributed in Mi-BCs (Fig. 4h, i, and Supplementary Fig. 4d, e, and Movie 6). We confirmed that another subunit of the ATP synthase complex, ATP5F1A, is also incorporated into Mi-BCs, suggesting that the entire ATP synthase may exist in Mi-BCs (Supplementary Fig. 6a, b). Although EGFP-cytochrome *c*, EGFP-ATP5F1A and EGFP-ATP5F1B co-localized with TagRFP-T-Mieap, they were excluded from the Mieap-containing phase and they accumulated in the Mieap-depleted phase in Mi-BCs. These results imply that CL-binding/related proteins are phase separated, but that they are incorporated into Mi-BCs in association with CL.

To determine whether Mieap binds directly to CL, we performed a fat blot assay⁴⁹, in which binding of GST-Mieap to CL, phosphatidylcholine (PC), and phosphatidylethanolamine (PE) was evaluated on lipid-dotted membranes. GST-Mieap bound to CL, but not to PC or PE (Fig. 4j).

Mi-BCs compartmentalize and facilitate CL metabolic reactions

We performed mass spectrometric analyses of CL in A549 cells with and without overexpression of Mieap by Ad-Mieap infection. The total amount of CL per cell was higher in Ad-Mieap infected cells than in cells without the infection (Fig. 5a). Broad CL species showed higher absolute values in cells infected with Ad-Mieap than in non-infected cells (Fig. 5b and Supplementary Data 1). In contrast, relative amounts of most CL species did not change. However, Mieap significantly increased the proportions of CL72:5, CL72:6, CL70:6, CL68:5, and CL68:6 (Fig. 5b). These results suggest that Mieap is involved in CL metabolism. Therefore, we speculated that Mi-BCs may function as MLOs to compartmentalize and facilitate CL metabolic reactions. To validate this hypothesis, we examined whether Mi-BCs phase-separate enzymes sequentially involved in CL metabolism (Fig. 5c).

Thus, we examined involvement of the following EGFP-tagged enzymes required for CL metabolism in Mi-BCs by performing confocal live-cell imaging: EGFP-TAMM41, EGFP-PGS1, EGFP-PTPMT1, and EGFP-CRLS1 (involved in CL biosynthesis); EGFP-PLA2G6 (related to CL hydrolysis by phospholipase A₂ activity); and EGFP-TAZ (involved in CL remodeling). All of these enzymes localized at mitochondria and were subsequently incorporated into Mi-BCs (Fig. 5d – i, and Supplementary Fig. 7a – f, and Movie 7). Interestingly, all of these CL metabolic enzymes tended to be concentrated in the Mieap-depleted phase in Mi-BCs (Fig. 5d – i, and Supplementary Movie 7).

We further examined three additional mitochondrial proteins, PRELI (EGFP-PRELI), mitochondrial protease LONP1 (EGFP-LONP1), and mitochondrial CL hydrolase/mitochondrial phospholipase (MitoPLD)/phospholipase D6 (EGFP-PLD6). PRELI is a mitochondrial carrier of PA for CL production²³. LONP1 is a AAA mitochondrial protease⁵⁰. PLD6 hydrolyzes CL to generate PA at the outer mitochondrial membrane⁵¹. EGFP-PRELI was incorporated into Mi-BCs (Fig. 5j, and Supplementary Fig. 7g and Movie 7), suggesting that Mi-BCs can also be supplied with PA as a substrate for CL synthesis (Fig. 5C). Both EGFP-LONP1 and EGFP-PLD6 were located at mitochondria, but neither was incorporated into Mi-BCs (Fig. 5k, l, and Supplementary Fig. 7h, i, and Movie 7).

Both N-terminal hydrophilic and C-terminal hydrophobic regions of Mieap are required to generate the multi-phase structure of Mi-BCs

Since CL biosynthetic enzymes and NAO are located at the inner mitochondrial membrane, we assumed that 3D imaging analysis of the relationship between Mi-BCs and enzymes/NAO would provide the most definitive information on the location of Mi-BCs at mitochondria.

Using fluorescence-tagged CL biosynthetic enzymes, we tried to confirm whether the enlarged Mi-BCs are truly localized within mitochondria by performing live-cell imaging analysis with tomographic 3D reconstruction. As shown in Fig. 6a and Supplementary Movies 8 and 10, enlarged Mi-BCs are fully enveloped by EGFP-TAMM41, signals of which are continuously localized from tubular mitochondria to

all around the surfaces of spherical Mi-BCs. Supporting the results of CL biosynthetic enzymes, we further confirmed that NAO is also continuously localized from tubular mitochondria, all round and inside of spherical Mi-BCs (Fig. 6b and Supplementary Movies 9 and 10).

Since EGFP-CRLS1 tends to localize at the surface of Mi-BCs, we compared signals of mApple-TOMM20 (the outer mitochondrial membrane) and EGFP-CRLS1 (the inner mitochondrial membrane) around Mi-BCs. As shown in Supplementary Fig. 8a – d, the signals of EGFP-CRLS1 were always detected inside the signals of mApple-TOMM20, compared to those of PLD6 (the outer mitochondrial membrane), suggesting that Mi-BCs are present within mitochondria, possibly facing the inner mitochondrial membrane at their surfaces. Similar results were obtained from the same analysis using another probe for EGFP-TAMM41 (Supplementary Fig. 8e).

Similarly, using EGFP-TAMM41 and NAO as mitochondrial probes, we determined whether Δ CC, Δ 275 and Δ 496 BCs are located inside mitochondria. As shown in Fig. 6c, e and Supplementary Movies 8 and 10, both Δ CC and Δ 496 BCs are also fully enveloped by EGFP-TAMM41, whose signals are continuously derived from tubular mitochondria. Moreover, Δ CC and Δ 496 BCs are also stained by NAO as a clear picture of tubular mitochondria and each condensate (Fig. 6f, h and Supplementary Movies 9 and 10). On the other hand, Δ 275 condensates are never related to the signals of EGFP-TAMM41 or NAO (Fig. 6d, g and Supplementary Movies 8 – 10). These results suggest that Δ CC and Δ 496 BCs are located inside mitochondria, whereas Δ 275 BCs are present outside mitochondria.

We further examined partitioning behaviors of WT, Δ CC, Δ 275, and Δ 496 proteins by performing analysis of Intensity Ratios (IRs) of each protein in BCs and cytoplasm⁵². As shown in Fig. 6i, IR values (condensates/cytoplasm) of WT, Δ CC, and Δ 496 are 158.62 ± 40.74 , 178.81 ± 34.07 , 8.29 ± 1.92 , and 153.14 ± 25.66 (mean \pm SD), respectively. This implies that IR of WT, Δ CC, and Δ 496 are more than 18 times higher than that of Δ 275. All WT, Δ CC, and Δ 496 BCs are localized within mitochondria, whereas Δ 275 condensates are present in cytoplasm. Therefore, these IR results suggest that Mieap protein tends to be highly partitioned and concentrated in mitochondrial BCs, and that this propensity is possibly determined by the C-terminal hydrophobic region of Mieap, which could mediate interaction of Mieap with CL/CL-related phospholipids.

To explore the mechanism responsible for multi-phase structure in Mi-BCs, using EGFP-TAMM41, we examined whether CL metabolic enzymes are phase-separated by Δ CC, Δ 275, and Δ 496 condensates (Fig. 7a – d). As expected, Δ 275 condensates did not phase-separate EGFP-TAMM41 (Fig. 7c). Importantly, although both Δ CC and Δ 496 are located in mitochondria, EGFP-TAMM41 was phase-separated and incorporated in the Mieap-depleted phase of Δ 496 condensates (Fig. 7d), whereas EGFP-TAMM41 was mainly localized across the surfaces of Δ CC condensates, which did not generate multi-phase structures (Fig. 7b). These results suggest that both the N-terminal hydrophilic and C-terminal hydrophobic regions are required to form multi-phase droplets. The region of IDR1-3 and two CCs may be critical to the interaction with CL metabolic enzymes to generate the internal enzyme-containing phase (the Mieap-deficient phase) in Mi-BCs.

We further explored the internal structure of the Mieap-depleted phase with EGFP-PGS1 or EGFP-TAMM41. Importantly, we found that CL biosynthetic enzymes, EGFP-PGS1 or EGFP-TAMM41, formed condensates in the Mieap-depleted phase, which wetted the interface between the Mieap-containing phase and the Mieap-depleted phase in either WT or $\Delta 496$ BCs (Fig. 7e – l). These results suggest that enzymatic reactions between CL metabolic enzymes and their substrates may occur at the interface between the Mieap-containing phase (Mieap and substrates) and the Mieap-depleted phase (CL metabolic enzymes).

Mieap functions in mitochondrial quality control via regulation of CL metabolism

CL alterations cause mitochondrial dysfunction^{22,25}. Mieap is thought to be involved in mitochondrial quality control^{29,30,32,35}. Therefore, we hypothesized that Mieap contributes to mitochondrial quality control by regulating CL metabolism. To test this hypothesis, we evaluated mitochondrial status relative to CL integrity in the presence or absence of Mieap protein in cells and mice.

First, we examined respiration rate, mitochondrial ATP production rate, crista morphology, and ROS levels, in control and Mieap-knockdown (KD) LS174T cells under physiological conditions, all of which reflect CL integrity. Flux analysis indicated that respiration and ATP production rates of Mieap-KD cells were significantly lower than those of control cells (Fig. 8a, b). TEM analysis revealed that cristae of Mieap-KD cells decreased, and their morphology became indistinct and irregular, compared to that of control cells (Fig. 8c, d). ROS levels increased in Mieap-KD cells (Supplementary Fig. 9). Consistently, the total amount of CL in control cells was higher than in Mieap-KD cells (Fig. 8e), and control cells showed higher absolute values for CL species than Mieap-KD cells (Fig. 8f and Supplementary Data 1). Furthermore, physiological Mieap significantly increased the relative values of CL72:4, CL72:5, CL70:4, CL68:3, and CL68:4 in LS174T cells (Fig. 8f).

Second, utilizing a Mieap-deficient colorectal cancer cell line HCT116²⁹, we examined whether overexpression of Mieap affects respiration rate and mitochondrial ATP production rate in these cells. As shown in Fig. 8g – j, overexpression of Mieap significantly enhanced respiration rate and mitochondrial ATP production in HCT116 cells.

Third, we analyzed crista morphology in kidney and liver tissues of Mieap-knockout (KO) mice by performing TEM analysis. In Mieap^{-/-} kidney mitochondria, irregularly dilated lamellar structures without distinct OsO₄ staining were observed (Fig. 8k). A decrease in normal crista structure was a common characteristic of Mieap^{-/-} mitochondria in the kidney and liver (Fig. 8k – n).

Fourth, we performed a large-scale cross-sectional observation of 1,225 Mieap^{+/+}, Mieap^{+/-}, and Mieap^{-/-} mice to identify long-term consequences of Mieap deficiency. Average body weights of Mieap^{+/-} and Mieap^{-/-} mice were higher than those of Mieap^{+/+} mice throughout their lives (Fig. 9a, b). Differences

were prominent during middle and old age, from 44 to 104 weeks (Fig. 9c) (mean value \pm SE; $Mieap^{+/+}$ 33.065 \pm 0.425 g [n=149], $Mieap^{+/-}$ 34.048 \pm 0.302 g [n=295], $Mieap^{-/-}$ 35.090 \pm 0.392 g [n=175]), but particularly during middle age, from 53 to 62 weeks (Fig. 9d) (mean value \pm SE; $Mieap^{+/+}$ 31.048 \pm 0.759 g [n=49], $Mieap^{+/-}$ 33.378 \pm 0.496 g [n=115], $Mieap^{-/-}$ 34.579 \pm 0.645 g [n=68]).

We further evaluated whether there is any difference in obesity between male and female in *Mieap*-deficient mice. As shown in Supplementary Fig. 10a, b, e, f, *Mieap*-deficient mice of both sexes developed obesity that persisted throughout their lives. This obesity was prominent during middle and old age, from 44 to 104 weeks (Supplementary Fig. 10c, g) (mean value \pm SE; $Mieap^{+/+}$ 36.060 \pm 0.509 g [n=74], $Mieap^{+/-}$ 36.835 \pm 0.371 g [n=139], $Mieap^{-/-}$ 37.679 \pm 0.461 g [n=90] in male, and $Mieap^{+/+}$ 30.110 \pm 0.514 g [n=75], $Mieap^{+/-}$ 31.565 \pm 0.356 g [n=156], $Mieap^{-/-}$ 32.350 \pm 0.483 g [n=85] in female), but more remarkably during middle age, from 53 to 62 weeks (Supplementary Fig. 10d, h), (mean value \pm SE; $Mieap^{+/+}$ 34.365 \pm 0.952 g [n=23], $Mieap^{+/-}$ 36.714 \pm 0.633 g [n=52], $Mieap^{-/-}$ 37.238 \pm 0.731 g [n=39] in male, and $Mieap^{+/+}$ 28.113 \pm 0.813 g [n=26], $Mieap^{+/-}$ 30.625 \pm 0.522 g [n=63], $Mieap^{-/-}$ 31.002 \pm 0.770 g [n=29] in female).

To confirm that the body weight gain in *Mieap*-deficient mice reflects increased fat deposition, we evaluated the amount of subcutaneous fat and intra-abdominal fat (perigonadal fat and perirenal fat) in four representative litter pairs ($Mieap^{+/+}$ and $Mieap^{-/-}$). As shown in Supplementary Fig. 11a – d, the amount of fat in $Mieap^{-/-}$ mice is obviously higher than in $Mieap^{+/+}$ mice in all four pairs. Therefore, we suggest that the body weight gain in *Mieap*-deficient mice is due to obesity.

Reduced mitochondrial respiratory activity in adipose tissues has been suggested as a factor contributing to obesity⁵³. Brown fat tissue (BAT) is essential to heat production via both its respiratory activity, which generates a proton gradient, and uncoupling protein 1 (UCP1)-mediated proton leakage across the mitochondrial inner membrane^{54,55}. Therefore, BAT mitigates obesity. Importantly, as a CL-binding protein, activity of UCP1 is stabilized by CL⁵⁶. Thus, we examined the status of mitochondrial cristae in BAT of $Mieap^{-/-}$ mice. We confirmed that normal crista structure was significantly decreased in *Mieap*-deficient BAT (Fig. 9e, f), suggesting that obesity may be a long-term consequence of mitochondrial dysfunction due to CL alteration in tissues of *Mieap*-deficient mice, including BAT.

Finally, we examined endogenous *Mieap* expression *in vivo*. To achieve this, utilizing WT, *Mieap*-KO, and p53-KO mice and anti-mouse *Mieap* antibody, we performed immunohistochemical (IHC) analysis on 20 tissues/organs, including brain (cerebellar cortex), brain (cerebroventricle), heart, liver, kidney, lung, stomach, small intestine, pituitary gland, eye, harderian gland, salivary gland, thyroid, bladder, testis, epididymis, seminal vesicle, prostate, uterus, and fallopian tube. Specific signals of *Mieap* were detected in all examined tissues/organs by comparing data from WT and *Mieap*-KO (Supplementary Fig. 12a – t). Interestingly, basal expression of endogenous *Mieap* protein is not regulated by p53. Importantly, patterns of *Mieap* expression are remarkably similar to those of cytochrome *c* in IHC and IF (Supplementary Fig. 12a – t), suggesting that endogenous *Mieap* protein is localized at mitochondria.

We further analyzed expression levels of endogenous Mieap in representative six tissues/organs, including testis, heart, kidney, liver, stomach, and lung, by western blot (WB). Although signals of endogenous Mieap were detected in all six tissues by IHC, we could not find specific bands in liver, kidney, heart, and stomach with WB (Supplementary Fig. 13a, b). Combined with results in IHC and WB, we suggest that physiological Mieap protein is expressed and localized in mitochondria in all tissues/organs, but its expression levels are low in most tissues/organs.

In IHC and WB, we confirmed that endogenous Mieap protein was highly expressed in testis. To validate whether fluorescence-tagged Mieap protein behaves identically to endogenous Mieap, using mNeonGreen-Mieap knock-in (KI) mice, we compared localization of mNeonGreen-tagged Mieap and endogenous Mieap in the testis. As shown in Supplementary Fig. 14a, b, mNeonGreen-tagged Mieap protein was detected at the midpiece of sperm in the testes of KI mice, localization of which was completely consistent with that of endogenous Mieap protein in B6 mice. This result suggests that fluorescence-tagged Mieap protein reflects the behavior of endogenous Mieap protein *in vivo*.

Considering the IR results, although endogenous Mieap protein is expressed at low levels in most tissues/organs, even low expression levels of Mieap protein could be highly concentrated in mitochondrial droplets under physiological conditions. This implies that physiological Mieap protein likely has a significant impact on mitochondrial quality control in all tissues/cells containing mitochondria. On the basis of all these results, we suggest that Mieap maintains mitochondrial quality by regulating CL metabolism.

Discussion

Although the importance of multi-enzyme complexes in metabolic enzyme reactions has been recognized, it remains unclear how this complex of enzymes efficiently and safely enables sequential enzymatic reactions by preventing diffusion of intermediates. A recent report suggested that concentration of multiple enzymes and substrates/intermediates in a restricted space could mediate efficient sequential enzymatic reactions by preventing diffusion of intermediates⁵⁷. In that model, multiple copies of upstream and downstream enzymes involved in sequential enzymatic reactions are assembled into a single cluster, called an “agglomerate.” According to this model, “once an upstream enzyme produces an intermediate, although the probability of the intermediate being processed by any individual downstream enzymes is low, the probability that the intermediate will be processed by one of the many downstream enzymes in the ‘agglomerate’ can be high.”⁵⁷ Therefore, based on this model, molecular crowding of enzymes, substrates, and intermediates in a restricted space could enable efficient sequential enzymatic reactions mediated by multiple enzymes.

The “agglomerate” concept is promising, but an important question remains. How can so many diverse molecules, including multiple enzymes, substrates, and intermediates, be gathered, concentrated, and compartmentalized in a single restricted space? What drives formation of the “agglomerate”? We speculate that BCs could organize agglomerates as metabolic BCs⁵⁸. Accumulating evidence suggests

that BCs function as MLOs, which promote biochemical reactions by concentrating and compartmentalizing enzymes and substrates in cells⁵⁹⁻⁶³. Since BCs are not surrounded by lipid bilayers, theoretically, they exhibit spatiotemporal dynamic properties within a cell in response to cellular stress and/or subcellular circumstances. More importantly, while BCs contain hundreds of molecules, a few scaffold proteins can drive formation of these MLOs¹. If there are proteins that can organize metabolic BCs as scaffolds⁶¹, these agglomerates could enable efficient metabolic reactions.

In the present study, we obtained the following evidence supporting our hypothesis that Mi-BCs may regulate CL metabolism: [1] Mieap drives formation of droplets in mitochondria. [2] Mi-BCs may phase-separate CL. [3] Mi-BCs phase-separate all four sequential enzymes for CL biosynthesis (TAMM41, PGS1, PTPMT1, and CRLS1). [4] Mi-BCs phase-separate two enzymes for CL remodeling (PLA2G6 and TAZ). [5] Mi-BCs phase-separate at least three CL-related proteins localized at or near the inner mitochondrial membrane (cytochrome *c*, PHB2, ATP5F1B, and ATP5F1A). [6] The presence or absence of Mieap protein is closely related to an increase or decrease in various species of CL, respectively. [7] Mieap protein specifically increases the proportion of several species of CLs. [8] Mieap deficiency is related to changes in crista structure and CL metabolism in cells, and crista structure *in vivo*. This evidence suggests that Mieap is a scaffold protein that drives formation of metabolic BCs to compartmentalize and concentrate enzymes, substrates, and intermediates that are involved in CL biosynthesis and remodeling, leading to molecular crowding within Mi-BCs that promotes efficient catalysis of CL metabolic reactions.

Mi-BCs exhibit properties of multi-phase droplets, in which there are two phases, a Mieap-containing phase and a Mieap-depleted phase. Interestingly, CL and Mieap occur in the Mieap-containing phase, whereas all CL biosynthesis and remodeling enzymes, including TAMM41, PGS1, PTPMT1, CRLS1, PLA2G6, and TAZ, are predominantly segregated into the Mieap-depleted phase. This result suggests that substrates, intermediates, and products for CL metabolism do not reside in the same phase as their catalytic enzymes. Such a relationship between substrates and enzymes in multi-phase droplets are not limited to Mi-BCs but seen in other droplets. In terms of RNA processing droplets formed by FMRP and CAPRIN1, RNA and phosphorylated FMRP form multi-phase droplets, in which the deadenylation enzyme, CNOT7, and the substrate, polyA-RNA, are segregated into different phases, but this leads to faster deadenylation rates¹⁷.

Why don't substrates and enzymes occur in the same phase of metabolic BCs? A recent study demonstrated that sequestration of enzymes to a membraneless compartment that is away from, but adjacent to substrates, can accelerate reactions much faster than when the enzymes are mixed with the substrates in the same compartment⁶⁴. Concentration of enzymes and substrates in a single phase might result in substrate inhibition⁶⁴. Therefore, separation of enzymes from their substrates via LLPS could facilitate enzymatic reactions by mitigating substrate inhibition. In this case, the interface between the enzyme and substrate phases would be the site of the reaction. Consistent with this hypothesis, we observed accumulation of CL biosynthetic enzymes such as PGS1 and TAMM41 at the interface of the Mieap-depleted phase (Fig. 7e – I). Therefore, enzymatic reactions of CL enzymes and CL substrates may

occur at the interface between the Mieap-containing phase (Mieap and substrates) and the Mieap-depleted phase (CL metabolic enzymes) (Fig. 10a – c).

Feric et al. reported the mechanism for generation of multi-phase structures in droplets⁶⁵. By performing *in vivo* and *in vitro* experiments, the authors demonstrated that layered droplet organization is caused by differences in droplet surface tension, facilitating sequential RNA processing reactions in a variety of RNP bodies. In their experiments, F1B and NPM1 formed multi-phase droplets in which F1B droplets tended to be encapsulated within NPM1 droplets. They found that F1B droplets tended to wet hydrophobic surfaces, whereas NPM1 droplets tended to wet hydrophilic surfaces. Wetting refers to the contact between liquids and surfaces, which depends on surface tension. Therefore, in the aqueous phase, F1B droplets with high surface tension tended to be enveloped by NPM1 droplets with lower surface tension.

Since Mieap may be positioned with its N-terminal domain facing outward at the surfaces of Mi-BCs (Supplementary Fig. 1c), Mi-BCs could exist in a hydrophilic environment. If so, according to the theory of Feric et al., the Mieap-containing phase may be enveloped by the Mieap-depleted phase, because the former is more hydrophobic than the latter. However, the authors also pointed out the presence of a surfactant that modulates surface tension alters or inverts the organization of multi-phase droplets. Since Mieap could serve as a biosurfactant, Mieap may modulate the surface tension of the Mieap-containing phase and the Mieap-depleted phase in a hydrophilic environment. Therefore, the relation between the two phases could be inverted in Mi-BCs.

We hypothesize the following model for sequential CL-metabolic reactions promoted by Mieap (Fig. 10a – c). Mieap may stably interact with the substrate (PA) via its C-terminal, hydrophobic, structured region, which exhibits a specific, strong interaction. On the other hand, Mieap weakly and transiently interacts with CL-metabolizing enzymes via its N-terminal hydrophilic region, which exhibits multiple interactions. In this model, once Mieap attracts the substrate with its C-terminal region, Mieap enables sequential CL metabolic reactions by transiently interacting with the enzyme corresponding to the substrate at the interface between the Mieap-containing phase and the Mieap-depleted phase, and then changing enzymes until mature CL is produced. Therefore, interactions of the N-terminal hydrophilic region of Mieap with CL enzymes and the C-terminal hydrophobic region of Mieap with CL/CL-related phospholipids may be critical to drive formation of multi-phase organization of Mi-BCs. In summary, (1) concentration of enzymes and substrates, (2) segregation of enzymes and substrates into distinct sub-compartments of metabolic droplets, (3) interfacial catalysis, and (4) biosurfactant activity of Mieap could foster highly efficient sequential enzymatic reactions for CL metabolism in Mi-BCs. We suggest that Mi-BCs may be the first known metabolic MLOs to regulate CL synthesis and remodeling.

BCs are often thought to accelerate enzymatic reaction rate by merely increasing local concentrations of enzymes and substrates (mass action). However, Peebles and Rosen reported that concentrating enzymes and substrates alone results in decreasing enzymatic reaction rates by substrate inhibition due to high concentrations of substrates¹⁸. They demonstrated that in addition to mass action, a scaffold-induced decrease in K_M is critical to accelerate enzymatic reactions in BCs¹⁸. In their synthetic system

where the SUMOylation enzyme cascade is recruited into engineered condensates, they showed that having both enzyme and substrate bound simultaneously to proximal sites in a scaffold oligomer, which leads to decreased K_M , is required to enhance the enzymatic reaction. Our Mi-BC model is compatible with their findings; however, further investigation of this hypothesis is required.

Significant evidence is now emerging to suggest a critical role of Mieap in mitochondrial quality control in response to cellular stresses. Under hypoxic conditions, Mieap-deficient gastric cancer cells exhibit abnormal mitochondrial structure, enhanced migration, and invasion via increased mitochondrial ROS generation³¹. Mieap expression is defective in oncocytic cell tumors of the thyroid, suggesting a causative role in accumulation of abnormal mitochondria in tumor cells³³. Oncocytic tumors are characterized by accumulation of abnormal mitochondria in tumor cells, but the underlying mechanism remains unclear. Recently, Mieap/Spata18 was reported to participate in DNA-damage-induced mitophagy⁶⁶. Results in these studies are largely consistent with our previous observations^{29,35}. However, all observations from these studies, as well as our previous work can be explained by the idea that Mieap influences mitochondrial quality control by regulating CL metabolism. The only unaddressed question is whether lysosomes/lysosomal proteins are involved in the function of Mieap. In response, we have now confirmed that EGFP-cathepsin D is localized at mitochondria and then incorporated into Mi-BCs (unpublished data). Although resolving this question will be challenging, we strongly suggest that the mechanism underlying these observations involves regulation of CL metabolism by Mieap.

In the present study, we demonstrated that Mieap-deficient LS174T cells exhibited altered CL metabolism, decreased respiration activity, increased ROS levels, and manifested abnormal crista structure, all of which are consistent with phenotypes induced by CL alteration. We also found that Mieap-deficient mice exhibit decreased numbers and morphological abnormalities of mitochondrial cristae in kidney and liver tissues. Furthermore, our body weight analysis of Mieap^{+/+}, Mieap^{+/-}, and Mieap^{-/-} mice clarified increased obesity in Mieap-deficient mice, which is likely attributable to mitochondrial dysfunction in various tissues, including BAT. Therefore, we assume that all these phenotypes in Mieap-deficient cells and mice reflect mitochondrial dysfunctions related to abnormal CL metabolism. So far, autophagy and proteostasis are two major mechanisms in mitochondrial quality control⁶⁷. In addition to these, we suggest that the Mieap-regulated pathway is the third mechanism for mitochondrial quality control, in which Mieap maintains integrity of mitochondria by regulating CL metabolism. It accomplishes this through homeostasis of the inner mitochondrial membrane by regulating CL metabolism, stabilizing oxidative phosphorylation, and suppressing mitochondrial ROS generation (Fig. 10d).

Previously, we reported that although Mieap-deficient mice did not suffer from intestinal dysfunction, Mieap-deficient Apc^{Min/+} mice exhibited remarkable intestinal tumor generation and malignant transformation, compared to Mieap-WT Apc^{Min/+} mice³². Furthermore, mitochondria in Mieap-deficient tumors revealed abnormal morphology, including fewer cristae and enlarged, spherical mitochondria. These results support the role of Mieap in mitochondrial quality control through control of CL metabolism in response to oncogenic stress. In addition to Apc^{Min/+} mice, we observed a similar effect in a Mieap-

deficient gastric cancer mouse model (unpublished data), using *K19-Wnt1/C2mE* transgenic mice⁶⁸. Therefore, Mieap-regulated mitochondrial quality control could be critical in tumor suppression by promoting CL metabolism, which leads to upregulation of respiratory activity and downregulation of mitochondrial ROS generation. Considering the role of Mieap in p53 function, we suggest that Mieap could act as a spatiotemporal and dynamic regulator/modulator of CL metabolism to suppress tumor initiation and progression. Recently, we found that Mieap-deficient sperm in Mieap-KO mice cause *in vitro* infertility due to mitochondrial ROS elevation and impaired sperm motility (unpublished data). Therefore, in addition to cancer and obesity, it is possible that alterations of Mieap-regulated mitochondrial quality control also promote infertility (Fig. 10d).

A recent study reported that PGS1, PTPMT1, and CRLS1 form a large mitochondrial CL synthesis complex in human cells, with a molecular mass of 700-800 kDa⁶⁹. This large CL synthesis complex includes multiple CL-binding proteins. These observations are very similar to our results that Mi-BCs contain all CL synthesis enzymes and several CL-binding proteins. However, IF experiments on PGS1 or CRLS1 in that study indicated that neither PGS1 nor CRLS1 showed visible Mi-BC-like structures in mitochondria⁶⁹. Our results from live-cell imaging of EGFP-fused CL synthesis enzymes, including PGS1 and CRLS1, also showed that none of the EGFP-tagged CL synthesis enzymes exhibit visible Mi-BC-like structures. Therefore, we suggest that under physiological conditions, the minute size of Mi-BCs or possibly layered, membraneless organelles induced by Mieap may compartmentalize and facilitate CL metabolic reactions *in vivo*, efficiently maintaining enzymatic reactions.

Supporting this hypothesis, although the expression levels of endogenous Mieap protein were low, we confirmed specific expression of Mieap protein *in vivo* in 20 tissues/organs that contain mitochondria (Supplementary Fig. 12a – t). Importantly, patterns of endogenous Mieap expression are very similar to those of cytochrome *c*, suggesting that endogenous Mieap protein is localized at mitochondria. On the other hand, the results of IR indicated that Mieap protein is highly concentrated in mitochondrial droplets (Fig. 6i). These results, taken together, imply that, although the physiological Mieap protein is expressed at low levels *in vivo*, it may be condensed into micro-Mi-BCs that are distributed all through mitochondria to promote CL metabolism. Therefore, we suggest that physiological Mieap protein may have a significant impact on mitochondrial quality control in all tissues/cells containing mitochondria. Further investigation is needed to clarify the full picture of physiological membraneless organelles involved in CL metabolism.

Materials And Methods

Cell lines

The following cell lines were purchased from the American Type Culture Collection: A549 (tissue, lung cancer; gender, male), U373MG (tissue, glioblastoma; gender, male), LS174T (tissue, colon cancer; gender, female), and 293 (tissue, embryonic kidney). A549 cells were cultured in RPMI 1640 (Sigma). U373MG, LS174T, and 293 cells were cultured in DMEM (Sigma). All media were supplemented with 10% fetal

bovine serum. Cells were maintained at 37°C in a humidified chamber with 5% CO₂. These cell lines have not been authenticated.

Mice

Animal experiment protocols were approved by the Committee for Ethics in Animal Experimentation (approved protocol No. T17-043), and experiments were conducted in accordance with Guidelines for Animal Experiments of the National Cancer Center. C57BL/6J WT mice were obtained from CLEA Japan (Tokyo, Japan). Mieap-knockout (Mieap^{-/-}) mice were generated using the Cre/loxP recombination system, as previously reported³². Briefly, floxed and trapped alleles were generated using a single construct bearing a gene-trap cassette doubly flanked by LoxP and FRT, located between exons 5 and 8 of the mouse Mieap gene, which is located on chromosome 5. Mieap homozygous (Mieap^{-/-}) deficient mice were generated by mating breeding pairs of Mieap heterozygous (Mieap^{+/-}) mice. p53-deficient mice were a gift from Dr. S. Aizawa, Center for Developmental Biology, RIKEN⁷⁰.

For generation of N-terminal or C-terminal mNeonGreen-tagged Mieap KI mice, targeting vectors containing the cassette of the 5'UTR-mNeonGreen-Linker-Exon1-intron1-FRT-NEO-FRT-intron1 or the intron10-exon11-intron11-exon12-intron12-exon13-Linker-mNeonGreen-FRT-NEO-FRT-3'UTR were constructed to express N-terminal or C-terminal mNeonGreen-tagged Mieap protein in mice, respectively. Targeting vectors were introduced into ES cells by electroporation. After geneticin selection, positive ES clones were screened by PCR and Southern blot analysis. The positive clones were injected into C57/B6 mouse blastocysts. The obtained heterozygous and homozygous mice were subjected to analysis.

All mice were housed at 22 ± 2°C with a 12 h light/dark cycle with free access to food, CE-2 (CLEA Japan), and water.

Establishment of KD cell lines

We established a Mieap-KD cell line using LS174T, as previously described²⁹. Mieap expression was inhibited in this cell line by retroviral expression of short-hairpin RNA (shRNA) against the Mieap sequence (Supplementary Fig. 15a, b). We also established LS174T-cont cells using a retroviral vector with a target sequence for EGFP, or an empty retroviral vector, and A549-cont cells using an empty retroviral vector.

Plasmid construction

Constructs containing Mieap

For construction of the plasmid containing N-terminal EGFP-tagged Mieap, the nucleotide sequence of Mieap was PCR-amplified using primers N-EGFP-Mieap-F and N-EGFP-Mieap-R. PCR products were digested with Kpn I and ligated into pEGFP-C1 (Clontech) cut with the same enzyme. For construction of the plasmid containing C-terminal EGFP-tagged Mieap, the nucleotide sequence of Mieap, excluding the stop codon, was PCR-amplified using the primers C-EGFP-Mieap-F and C-EGFP-Mieap-R. PCR products were ligated into the pCR-Blunt II-TOPO vector (Thermo Fisher Scientific) and sequenced. Inserted products were excised using Hind III restriction sites, and ligated into pEGFP-N1 (Clontech), cut with the same enzyme. N-terminal EGFP-tagged Mieap was used as EGFP-Mieap, except for Fig. 1a – d and Supplementary Movie 3 where the C-terminal EGFP-tagged Mieap was used.

Plasmids containing N-FLAG-Mieap (pN-FLAG-Mieap) were constructed as follows. The nucleotide sequence of Mieap was PCR-amplified using the primers, N-FLAG-Mieap-F and N-FLAG-Mieap-R. PCR products were ligated into the pCR-Blunt II-TOPO vector (Thermo Fisher Scientific) and sequenced. Inserted products were excised using the Kpn I restriction sites and ligated into pre-digested pcDNA3.1 (+) (Thermo Fisher Scientific) cut with the same enzyme. The nucleotide sequence of Mieap was excised from the plasmid using the Hind III and Xho I restriction sites, and ligated into pre-digested pCMV-Tag2A (Agilent) cut with the same enzyme.

The plasmid containing C-FLAG-Mieap (pC-FLAG-Mieap) was constructed as follows. The nucleotide sequence of Mieap, excluding the stop codon, was PCR-amplified using the primers, C-EGFP-Mieap-F and C-EGFP-Mieap-R, the same primers used for construction of the plasmid containing C-terminal EGFP-tagged Mieap. PCR products were ligated into the pCR-Blunt II-TOPO vector (Thermo Fisher Scientific) and sequenced. Inserted products were excised using the Hind III restriction site and ligated into pre-digested p3xFLAG-CMV-14 (Sigma Aldrich) cut with the same enzyme.

Prior to construction of plasmids containing EGFP-Mieap deletion mutants, point mutations in Bgl II, Sac I, EcoR I, and Pst I restriction sites of the multiple cloning site of pEGFP-Mieap were introduced using QuikChange Site-Directed Mutagenesis Kits (Agilent) with primers Mut-F1, Mut-R1, Mut-F2 and Mut-R2, which were confirmed by DNA sequencing.

For construction of plasmids containing EGFP-Mieap Δ CC (pEGFP-Mieap Δ CC), the nucleotide sequence of pEGFP-Mieap between two Pst I restriction sites was deleted by digestion with Pst I. The remainder was self-ligated, additionally deleting c.810C using the QuikChange Site-Directed Mutagenesis Kit (Agilent) with primers Mut-F3 and Mut-R3 to make the deletion mutation in-frame.

For construction of plasmids containing EGFP-Mieap Δ 275 (pEGFP-Mieap Δ 275), the nucleotide sequence of pEGFP-Mieap between the Bgl II and Sma I restriction sites was deleted by digestion using Bgl II and Sma I. After blunting with T4 DNA polymerase (Thermo Fisher Scientific), the remainder was self-ligated.

For construction of plasmids containing EGFP-Mieap Δ 496 (pEGFP-Mieap Δ 496), the nucleotide sequence of pEGFP-Mieap was deleted between the EcoR I and Kpn I restriction sites by digestion using EcoR I and Kpn I. After blunting with T4 DNA polymerase (Thermo Fisher Scientific), the remainder was self-ligated.

For construction of plasmids containing TagRFP-T-Mieap (pTagRFP-T-Mieap), the nucleotide sequence of pEGFP-Mieap between the Nhe I and Xho I restriction sites containing EGFP was replaced with nucleotide sequence of pTagRFP-T-EEA1 (Addgene #42635) between the Nhe I and Xho I restriction sites containing TagRFP-T, by digestion using Nhe I and Xho I.

For construction of plasmids containing GST-Mieap (pGST-Mieap), the nucleotide sequence of Mieap (amino acids 99-298) was PCR-amplified using the primers, GST-Mieap-F and GST-Mieap-R. PCR products were ligated into the pCR-Blunt II-TOPO vector (Thermo Fisher Scientific) and sequenced. Products were digested with EcoR I and Xho I, and ligated into pGEX5X-2 (Cytiva).

For construction of plasmids containing Mieap Δ CC (pMieap Δ CC), pEGFP-Mieap Δ CC was digested at the Kpn I restriction sites to obtain the nucleotide sequence of Mieap Δ CC, and ligated into pcDNA3.1 (+) (Thermo Fisher Scientific) cut with the same enzyme, Kpn I.

For construction of plasmids containing Mieap Δ 274 (pMieap Δ 274), the nucleotide sequence of Mieap Δ 274 was PCR-amplified from pEGFP-Mieap Δ 275 using the primers, Δ 274-F and Δ 274-R. PCR products were digested with Kpn I, and ligated into pcDNA3.1 (+) (Thermo Fisher Scientific) cut with the same enzyme, Kpn I.

For construction of plasmids containing Mieap Δ 496 (pMieap Δ 496), pEGFP-Mieap Δ 496 was subjected to inverse PCR using the primers, Δ EGFP-F and Δ EGFP-R to delete the nucleotide sequence of EGFP from pEGFP-Mieap Δ 496, and the product was self-ligated using KOD-Plus-Mutagenesis Kit (TOYOBO).

Prior to construction of plasmids containing TagRFP-T-Mieap deletion mutants, the nucleotide sequence of TagRFP-T was PCR-amplified using the primers, TagRFP-T-F and TagRFP-T-R. PCR products were digested with Hind III and EcoR V, and ligated into pcDNA3.1 (+) (Thermo Fisher Scientific) cut with the same enzymes (pcDNA-N-TagRFP). The nucleotide sequence of Mieap was PCR-amplified using the primers, G35-F and G35-R. PCR products were digested with EcoRV and PspOMI, and ligated into pcDNA-N-TagRFP cut with the same enzymes (pG35).

For construction of plasmids containing TagRFP-T-Mieap Δ CC (pTagRFP-T-Mieap Δ CC), pG35 was subjected to inverse PCR using the primers, Δ CC-F and Δ CC-R, and the product was self-ligated using KOD-Plus-Mutagenesis Kit (TOYOBO).

For construction of plasmids containing TagRFP-T-Mieap Δ 275 (pTagRFP-T-Mieap Δ CC), pTagRFP-T-Mieap was subjected to inverse PCR using the primers, Δ 275-F and Δ 275-R, and the product was self-ligated using KOD-Plus-Mutagenesis Kit (TOYOBO).

For construction of plasmids containing TagRFP-T-Mieap Δ 496 (pTagRFP-T-Mieap Δ 496), pG35 was subjected to inverse PCR using the primers, Δ 496-F and Δ 496-R, and the product was self-ligated using KOD-Plus-Mutagenesis Kit (TOYOBO).

All primers are listed in Supplementary Data 2.

Other constructs

For construction of plasmids containing EGFP-BNIP3 (pEGFP-BNIP3), plasmids containing FLAG-BNIP3 (pCMV-Tag2B-BNIP3) were constructed in advance. For construction of the pCMV-Tag2B-BNIP3, the nucleotide sequence of BNIP3 was PCR-amplified using the primers, BNIP3-F and BNIP3-R. PCR products were ligated into the pCR-Blunt II-TOPO vector (Thermo Fisher Scientific) and sequenced. Inserted products were digested with EcoR I and Xho I, and ligated into the pre-digested pCMV-Tag2B (Agilent) cut with the same enzyme. The nucleotide sequence of pCMV-Tag2B-BNIP3 was digested at the EcoR I and Xho I restriction sites, and subsequently blunted with T4 DNA polymerase (Thermo Fisher Scientific). pEGFP-C1 (Clontech) was digested with Bgl II, blunted with T4 DNA polymerase, self-ligated, digested with EcoR I and Sma I, and ligated with the fragment of pCMV-Tag2B-BNIP3.

For construction of plasmids containing EGFP-NIX (pEGFP-NIX), plasmids containing FLAG-NIX (pCMV-Tag2B-NIX) were constructed in advance. For construction of the pCMV-Tag2B-NIX, the nucleotide sequence of NIX was PCR-amplified using the primers, NIX-F and NIX-R. PCR products were ligated into the pCR-Blunt II-TOPO vector (Thermo Fisher Scientific) and sequenced. Inserted products were digested with EcoR I and Xho I, and ligated into pre-digested pCMV-Tag2B (Agilent) cut with the same enzyme. The nucleotide sequence of pCMV-Tag2B-NIX was digested at the EcoR I and Xho I restriction sites, and subsequently blunted with T4 DNA polymerase (Thermo Fisher Scientific). pEGFP-C1 (Clontech) was digested with Bgl II, blunted with T4 DNA polymerase, self-ligated, digested with EcoR I and Sma I, and ligated with the fragment of pCMV-Tag2B-NIX.

Plasmids containing EGFP-cytochrome *c* (pEGFP-cytochrome *c*) were constructed as follows. The nucleotide sequence of cytochrome *c* was PCR-amplified using the primers (Cytochrome *c*-F and Cytochrome *c*-R) as reported by Goldstein et al.⁷¹. PCR products were ligated into the pCR-Blunt II-TOPO vector (Thermo Fisher Scientific) and sequenced. Inserted products were excised using the EcoR I and BamH I restriction sites, and ligated into pEGFP-C1 (Clontech) cut with the same enzymes.

For construction of the plasmid backbone containing EGFP (pN-EGFP), the nucleotide sequence of EGFP, excluding the stop codon, was PCR-amplified using the primers, N-EGFP-F and N-EGFP-R. PCR products were digested with Hind III and BamH I, and ligated into pcDNA3.1 (+) (Thermo Fisher Scientific) cut with the same enzymes.

For construction of the plasmid backbone containing EGFP (pC-EGFP), the nucleotide sequence of EGFP was PCR-amplified using the primers, C-EGFP-F and C-EGFP-R. PCR products were digested with BamH I and Not I, and ligated into pcDNA3.1 (+) (Thermo Fisher Scientific) cut with the same enzymes.

For construction of plasmids containing EGFP-ATP5F1B (pEGFP-ATP5F1B), the nucleotide sequence of ATP5F1B, excluding the stop codon, was PCR-amplified using the primers, ATP5F1B-F1, ATP5F1B-R1, ATP5F1B-F2, and ATP5F1B-R2. PCR products were digested with Hind III and BamH I and ligated into pC-EGFP cut with the same enzymes.

For construction of plasmids containing EGFP-PHB2 (pEGFP-PHB2), the nucleotide sequence of PHB2, excluding the stop codon, was PCR-amplified using the primers, PHB2-F and PHB2-R. PCR products were digested with Nhe I and Kpn I and ligated into pC-EGFP cut with the same enzymes.

For construction of plasmids containing EGFP-ATP5F1A (pEGFP-ATP5F1A), the nucleotide sequence of ATP5F1A, excluding the stop codon, was PCR-amplified using the primers, ATP5F1A-F and ATP5F1A-R. PCR products were digested with Nhe I and Hind III and ligated into pC-EGFP cut with the same enzymes.

For construction of plasmids containing EGFP-TAMM41 (pEGFP-TAMM41), the nucleotide sequence of TAMM41, excluding the stop codon, was PCR-amplified using the primers, TAMM41-F and TAMM41-R. PCR products were digested with Nhe I and BamH I, and ligated into pC-EGFP cut with the same enzymes.

For construction of plasmids containing EGFP-PGS1 (pEGFP-PGS1), the nucleotide sequence of PGS1, excluding stop codon, was PCR-amplified using the primers, PGS1-F and PGS1-R. PCR products were digested with Hind III and BamH I and ligated into pC-EGFP cut with the same enzymes.

For construction of plasmids containing EGFP-PTPMT1 (pEGFP-PTPMT1), the nucleotide sequence of PTPMT1, excluding the stop codon, was PCR-amplified using the primers, PTPMT1-F and PTPMT1-R. PCR products were digested with Nhe I and Hind III and ligated into pC-EGFP cut with the same enzymes.

For construction of plasmids containing EGFP-CRLS1 (pEGFP-CRLS1), the nucleotide sequence of CRLS1 was PCR-amplified using the primers, CRLS1-F and CRLS1-R. PCR products were digested with BamH I and Not I and ligated into pN-EGFP cut with the same enzymes.

For construction of plasmids containing EGFP-PLA2G6 (pEGFP-PLA2G6), the nucleotide sequence of PLA2G6, excluding the stop codon, was PCR-amplified using the primers, PLA2G6-F and PLA2G6-R. PCR products were digested with Nhe I and Kpn I and ligated into pC-EGFP cut with the same enzymes.

For construction of plasmids containing EGFP-TAZ (pEGFP-TAZ), the nucleotide sequence of TAZ, excluding the stop codon, was PCR-amplified using the primers, TAZ-F and TAZ-R. PCR products were digested with Nhe I and Kpn I and ligated into pC-EGFP cut with the same enzymes.

For construction of plasmids containing EGFP-PRELI (pEGFP-PRELI), the nucleotide sequence of PRELI, excluding the stop codon, was PCR-amplified using the primers, PRELI-F and PRELI-R. PCR products were digested with Nhe I and BamH I and ligated into pC-EGFP cut with the same enzymes.

For construction of plasmids containing EGFP-LONP1 (pEGFP-LONP1), the nucleotide sequence of LONP1, excluding the stop codon, was PCR-amplified using the primers, LONP1-F and LONP1-R. PCR

products were digested with Hind III and BamH I and ligated into pC-EGFP cut with the same enzymes.

For construction of plasmids containing EGFP-PLD6 (pEGFP-PLD6), the nucleotide sequence of PLD6, excluding the stop codon, was PCR-amplified using the primers, PLD6-F and PLD6-R. PCR products were digested with Nhe I and Kpn I and ligated into pC-EGFP cut with the same enzymes.

All primers are listed in Supplementary Data 2.

Transfection

For transfection, cells were seeded (2×10^5 cells/dish) in 35-mm glass bottom dishes. Plasmids (2 μ g /dish) were transfected using FuGENE6 transfection reagent (Promega), according to the manufacturer's instructions.

Recombinant adenovirus construction

Ad-Mieap was derived from viruses as previously reported^{29,35,72}. Replication-deficient recombinant viruses Ad-EGFP-Mieap, Ad-N-FLAG-Mieap, Ad-C-FLAG-Mieap, Ad-EGFP-Mieap Δ CC (Δ 104-270), Ad-EGFP-Mieap Δ 275, Ad-EGFP-Mieap Δ 496, Ad-TagRFP-T-Mieap, Ad-mApple-TOMM20 derived from mApple-TOMM20-N-10 (Addgene #54955), Ad-EGFP-BNIP3, Ad-EGFP-NIX, Ad-AcGFP1-Mito, Ad-DsRed2-Mito, and Ad-EGFP-cytochrome *c* were generated from the corresponding plasmid vectors and purified as described previously⁷³. Briefly, DNA fragments obtained by restriction of each plasmid vector were blunted using T4 DNA polymerase, ligated into the SmaI site of the cosmid, pAxCawtit (Takara), which contains the CAG promoter and the entire genome of type 5 adenovirus, except the E1 and E3 regions. Recombinant adenoviruses were generated by *in vitro* homologous recombination in the 293 cell line with the cDNA-inserted pAxCawtit and the adenovirus DNA terminal–protein complex. Viruses were propagated in the 293 cell line and purified by two rounds of CsCl density centrifugation. Viral titers were determined with a limiting dilution bioassay using 293 cells.

Adenoviral infection

Infection of cell lines was carried out by adding viral solutions to cell monolayers, incubating them at 37°C for 120 min with brief agitation every 20 min. This was followed by addition of culture medium and return of the infected cells to the 37°C incubator.

Immunocytochemistry

For immunocytochemistry, cells were grown on 8-well chamber slides ($1-4 \times 10^4$ cells/well) at 37°C in conventional culture medium, and fixed in paraformaldehyde (Supplementary Fig. 1b, 2%; Supplementary Fig. 1c, 4%) for 15 min at room temperature. Slides were incubated with Triton X-100 (Supplementary Fig. 1b, 0.1% for 2 min; Supplementary Fig. 1c, 0.5% for 10 min), and washed 3x with phosphate-buffered saline (PBS) at room temperature. Cells were blocked with 3% bovine serum albumin (BSA) in PBS (Supplementary Fig. 1b, for 3 h; Supplementary Fig. 1c, for 2 h), and sequentially incubated with rabbit polyclonal anti-Mieap antibody (1:200), mouse monoclonal anti-GFP antibody (1:200), or mouse monoclonal anti-FLAG antibody (1:1000) for 2 h at room temperature. After washing 3x with PBS, slides were incubated with Alexa Fluor 546 goat anti-rabbit IgG antibody (1:200) or Alexa Fluor 546 goat anti-mouse IgG antibody (1:200) at room temperature (Supplementary Fig. 1b, for 2 h; Supplementary Fig. 1c, for 1 h). Slides were washed 3x with PBS. Then they were mounted with VECTASHIELD H-1000 (Vector Laboratories) and observed using a FLUOVIEW FV3000 confocal laser scanning microscope (Olympus).

Histological analysis

Hematoxylin and eosin (HE) staining was performed using Eosin (CS701, Dako) and Hematoxylin (S2020, Dako). Immunohistochemistry (IHC) was performed as described previously³². Briefly, for antigen retrieval, paraffin-fixed sections were autoclaved in citric acid buffer (pH 6.0) at 121°C for 10 min. Sections were treated with 0.3% hydrogen peroxide in methanol for 30 min at room temperature to block endogenous peroxidase activity and incubated with 5% bovine serum albumin (BSA) in 50 mM Tris-buffered saline (pH 7.4) containing 0.05% Triton X-100 (T-TBS) for 1 h at room temperature to block non-specific protein binding sites. Sections were then incubated at 4°C with the primary antibodies, rabbit polyclonal anti-mouse Mieap antibody (1:1000)³², and mouse monoclonal anti-cytochrome *c* (ab13575, 1 $\mu\text{g}/\text{mL}$) in TBS-T. After overnight incubation, sections were incubated with EnVision + Dual Link System-HRP reagents (Dako) for 1 h according to the manufacturer's instructions at room temperature and treated with 0.02% DAB (DOJINDO) in 0.05 M Tris-HCl buffer (pH 7.6). Finally, sections were counterstained with Hematoxylin (Dako). For immunofluorescence (IF), rabbit polyclonal anti-mouse Mieap antibody (1:1000)³², and mouse monoclonal anti-cytochrome *c* (ab13575, 1 $\mu\text{g}/\text{mL}$) were used for primary antibodies. Alexa Fluor 594 goat anti-rabbit IgG antibody (1:200) and Alexa Fluor 488 goat anti-mouse IgG antibody (1:100) were used for secondary antibodies. Nuclear staining was performed with Hoechst 33342 (10 $\mu\text{g}/\text{mL}$) or TO-PRO-3 (200 nM).

Transmission electron microscopy (TEM)

A549-cont and U373MG cells (4×10^4 cells/24-well plate) were infected with Ad-Mieap. On day 1 after infection, cells were fixed in phosphate buffered 2.5% glutaraldehyde and subsequently post-fixed in 1%

OsO₄ at 4°C for 2 h. Then, specimens were dehydrated in a graded ethanol series and embedded in epoxy resin. Ultrathin sections (75 nm) were cut with an ultramicrotome. Ultrathin sections stained with uranyl acetate and lead staining solution were observed on a transmission electron microscope H-7500 (Hitachi) at 80 kV.

LS174T (control and Mieap-KD) cells cultured under normal conditions were also processed for TEM as mentioned above, with the following modifications. 2% glutaraldehyde was used for prefixation. 2% OsO₄ was used instead for post-fixation. 80-90-nm ultrathin sections were cut and observed on a transmission electron microscope H-7600 (Hitachi) at 100 kV.

Kidney and liver specimens were collected from an 18-week-old WT mouse and a 16-week-old Mieap^{-/-} male mouse. BAT specimens were collected from a 40-week-old WT and a 40-week-old Mieap^{-/-} male mouse. Specimens cut into approximately 3 × 3 × 3 mm³ were also processed for TEM and processed in the same fashion as the aforementioned A549-cont cells. However, a mixture of 2% paraformaldehyde and 2% glutaraldehyde was used for prefixation.

Post-embedding immunoelectron microscopy

A549-cont cells (2×10⁵ cells/35-mm glass bottom dish) were infected with Ad-Mieap. On day 1 after infection, cells were fixed with 4% paraformaldehyde and 0.025% glutaraldehyde in 0.1 M PBS (pH 7.4) for 1 h at 4°C. After fixation, cells were washed with 0.1 M PBS (pH 7.4) for 16 h at 4°C, dehydrated in a graded ethanol series, and infiltrated with LR White resin. Polymerization was performed in TAAB embedding capsules (TAAB) inverted on glass-bottom dishes for 3h at 60°C. Ultrathin sections (75 nm) were collected on nickel grids. After blocking with 3% BSA in PBS for 1 h, sections were incubated with anti-Mieap antibody (1:200) diluted in PBS with 0.05% Triton X-100 for 2h at RT. Sections were washed 8x with 0.15% glycine in PBS, and incubated with goat anti-rabbit IgG 10-nm gold antibody (1:50) diluted in PBS with 0.05% Triton X-100 for 2h at RT. Sections were washed 8x in PBS and fixed with 1% glutaraldehyde in PBS for 5 min. Sections were washed 8x in distilled water. Grids were embedded in a mixture containing 2.7% polyvinyl alcohol and 0.3% uranyl acetate. Sections on grids were observed on a transmission electron microscope H-7500 (Hitachi) at 75 kV.

Amino acid sequence analyses of Mieap protein

We analyzed the phylogenetic spread of Mieap orthologs using OrthoDB v10 (<https://www.orthodb.org/>)³⁷. Multiple sequence alignment for Mieap orthologs was performed using Genetyx ver. 10. Prediction of IDRs in the amino acid sequence of Mieap was done using VL3-BA³⁹ on the PONDR server (<http://www.pondr.com/>) and collated with meta-prediction of IDRs using DisMeta (<http://www-nmr.cabm.rutgers.edu/bioinformatics/disorder/>)³⁸. Prediction of coiled-coil regions was

done using COILS (https://embnet.vital-it.ch/software/COILS_form.html)⁴⁰. Hydrophobicity of Mieap was analyzed according to the Kyte-Doolittle index⁴² using ProtScale (<https://web.expasy.org/protscale/>)⁷⁴. The linear net charge per residue of Mieap was analyzed using CIDER (<http://pappulab.wustl.edu/CIDER/>)⁴¹.

Analyses of confocal microscopy image data

Throughout the study, confocal microscopy images were taken with a FLUOVIEW FV3000 confocal laser scanning microscope (Olympus). For validation of the spatial relationship between Mi-BCs and mApple-TOMM20, additional images were taken using a SpinSR10 spinning disk confocal super resolution microscope (Olympus). For Z-stack and time-lapse imaging, a montage of differential interference contrast (DIC) and fluorescence images was created using MetaMorph ver. 7.8 (Molecular Devices). 3D reconstruction was performed using cellSens Imaging Software (Olympus). Line-scan profiles were acquired using MetaMorph ver. 7.8 (Molecular Devices).

FRAP experiments

EGFP-Mieap, EGFP-Mieap Δ CC, EGFP-Mieap Δ 275, and EGFP-Mieap Δ 496 were expressed in A549-cont cells to generate condensates by infection with Ad-EGFP-Mieap, Ad-EGFP-Mieap Δ CC, Ad-EGFP-Mieap Δ 275, and Ad-EGFP-Mieap Δ 496, respectively. FRAP experiments were performed on a FLUOVIEW FV3000 confocal laser scanning microscope (Olympus), using a 60x/1.4 NA oil immersion objective (Olympus). Condensates were subjected to spot-bleaching or full-bleaching (bleaching entire condensates). For spot-bleaching, the bleaching area was unified to a diameter of 1.38 μ m. Condensates were imaged for 6 s, acquiring 30 images prior to spot-bleaching or 50 s, acquiring 5 images prior to full-bleaching. Photobleaching employed a 488-nm laser at 10% laser power with 11.6 μ s/ μ m exposure time or 1.4% laser power with 1.4 μ s/ μ m exposure time. Time-lapse images were acquired at 0.2-ms intervals for 60 s or 10 s intervals for 15 min. Spot-bleaching data for each construct were acquired from 15 different condensates. Full-bleaching data of each construct were acquired from 10 different condensates.

Calculation of intensity ratio (IR)

To evaluate partitioning of EGFP-Mieap and deletion mutant proteins, EGFP-Mieap WT, Δ CC, Δ 275, and Δ 496 were expressed in A549-cont cells to generate condensates by infection with Ad-EGFP-Mieap WT, Δ CC, Δ 275, and Δ 496, respectively. EGFP intensity of condensates and cytoplasm was measured. Because EGFP intensity of these condensates was higher than the intensity of 0.4 mg/mL His-EGFP solution for standard curve, we chose intensity ratio (IR) rather than partition coefficient (PC) for the

parameter of this partitioning experiments⁵². IR was calculated as $(I_{\text{condensates}} - I_{\text{background}}) / (I_{\text{cytoplasm}} - I_{\text{background}})$, where $I_{\text{condensates}}$, $I_{\text{cytoplasm}}$, and $I_{\text{background}}$ are the mean intensities of condensates, cytoplasm, and PBS acquired by the identical conditions (laser wavelength, 488 nm; laser transmissivity, 0.01%; detection wavelength, 500–600 nm; voltage, 350 V) on a FLUOVIEW FV3000 confocal laser scanning microscope (Olympus). IR data were obtained from 40 cells for each construct.

Expression and purification of GST and GST-Mieap

Escherichia coli (BL21) cells transformed with expression vectors were grown in 200 mL of Luria-Bertani medium at 37°C until the OD₆₀₀ was between 0.55-0.6. Protein expression was induced with 100 μM IPTG, and bacteria were subsequently incubated for 3 h at 25°C. After harvesting bacteria by centrifugation at 3000 × *g* for 10 min at 4 °C, pellets were lysed with lysis buffer (1% Triton X-100 buffered in PBS supplemented with 1 mM Phenylmethylsulfonyl fluoride), and sonicated (20 × 30 s bursts with 10 s rest between bursts). Insoluble material was removed by centrifugation at 10,000 rpm for 30 min at 4 °C. Supernatant was incubated with glutathione-Sepharose 4B (Cytiva) pre-equilibrated with lysis buffer at 4°C overnight. After the beads were washed twice with lysis buffer, proteins were eluted with elution buffer (50 mM glutathione diluted in 50 mM Tris–HCl, pH 8.0), and dialyzed at 4°C overnight against PBS.

Lipid-binding analysis

For lipid-binding analysis, protein-lipid interactions on lipid-spotted membranes were evaluated with fat blot assays⁴⁹. Natural CL, PC, and PE derived from bovine heart (Olbracht Serdary Research Laboratories) were diluted with chloroform/methanol/1N HCl (80:80:1). 1 μL of each diluted lipid was spotted onto PVDF membranes (Cytiva) for antigen-antibody reactions using anti-Mieap antibody or nitrocellulose membranes (Cytiva) for antigen-antibody reactions using an anti-GST antibody to align spots with increasing amounts of lipids ranging from 0-667 pmol. Here, approximate molarities of CL, PC, and PE calculated from molecular weights of tetralinoleoyl CL, distearoyl PC, and distearoyl PC were used, respectively. After membranes were blocked with blocking buffer (3% fatty acid-free BSA diluted in 50 mM Tris–HCl, 150 mM NaCl, pH 7.5) for 1 h, membranes were incubated with 2.5 μg/mL of GST-Mieap or GST protein diluted in blocking buffer containing 0.1% Tween 20 overnight. Membranes were incubated with primary antibody (rabbit anti-Mieap antibody or rabbit anti-GST antibody) diluted in blocking buffer containing 0.06% Tween 20 (1:1000) for 3.5 h, and subsequently a secondary antibody (goat anti-rabbit antibody conjugated to horseradish-peroxidase) diluted in blocking buffer containing 0.06% Tween 20 (1:10000) for 1 h. ECL Western Blotting Detection Reagents (Cytiva) was used to detect HRP and chemiluminescence was visualized with an ImageQuant LAS 4000 system (Cytiva).

Lipid preparation

Lipid preparation was performed as described previously^{75,76}. Briefly, total lipids were extracted from samples using the Bligh-Dyer method⁷⁷. An aliquot of the organic phase was added to an equal volume of methanol before being loaded onto a DEAE-cellulose column (Wako Chemical) pre-equilibrated with chloroform. After successive washes with chloroform/methanol (1:1, v/v), acidic phospholipids were eluted with chloroform/methanol/HCl/water (12:12:1:1, v/v), followed by evaporation to dryness to yield a residue was soluble in methanol.

Mass spectrometric analyses of CL

Analyses were performed on an LC/MS/MS system consisting of a Q-Exactive Plus mass spectrometer (Thermo Fisher Scientific) equipped with an electrospray ionization source and an UltiMate 3000 system (Thermo Fisher Scientific). Lipid samples were separated on a Waters X-Bridge C₁₈ column (3.5 μm, 150 mm × 1.0 mm i.d.) at 40°C using a solvent step-gradient as follows: mobile phase A (isopropanol/methanol/water (5:1:4, v/v/v) supplemented with 5 mM ammonium formate and 0.05% ammonium hydroxide (28% in water))/mobile phase B (isopropanol supplemented with 5 mM ammonium formate and 0.05% ammonium hydroxide (28% in water)) ratios of 60%/40% (0 min), 40%/60% (1 min), 20%/80% (9 min), 5%/95% (11-30 min), 95%/5% (31-35 min) and 60%/40% (45 min). Flow rate was 25 μL/min. Source and ion transfer parameters applied were as follows. Spray voltage was 3.0 kV. For negative ionization modes, the sheath gas and capillary temperatures were maintained at 60 and 320 °C, respectively. The Orbitrap mass analyzer was operated at a resolving power of 70,000 in full-scan mode (scan range: 200–1800 m/z; automatic gain control (AGC) target:3e6) and of 35,000 in the Top 20 data-dependent MS2 mode (stepped normalized collision energy: 20, 30 and 40; isolation window: 4.0 m/z; AGC target: 1e5). Identification of CL molecular species was performed using LipidSearch 4.2 software (Mitsui Knowledge Industry).

Real-time ATP rate assay

LS174T-cont and Mieap-KD cells were seeded at a density of 2.5×10^4 cells/well (n=9) on a Seahorse XF24 Cell Culture Microplate. Cells were incubated at 37°C in a humidified chamber with 5% CO₂. 18 h after seeding, culture medium was replaced with XF DMEM medium pH 7.4 supplemented with 25 mM glucose and 2 mM L-glutamine through three washes.

HCT116 cells were seeded at a density of 0.8×10^6 cells/60-mm dish (n=9). Cells were incubated at 37°C in a humidified chamber with 5% CO₂. 24 h after seeding, cells were treated with Ad-Mieap or Ad-empty. 24 h after infection, cells were reseeded at a density of 4×10^4 cells/well (n=9) on a SeahorseXF24 Cell

Culture Microplate. 20 h after reseeding, culture medium was replaced with XF DMEM medium pH 7.4 supplemented with 25 mM glucose and 2 mM L-glutamine through three washes.

After cells were incubated at 37 °C in a non-CO₂ incubator for 60 min, cell culture plates were loaded into a Seahorse XFe24 Analyzer. Oxygen consumption rate (OCR) and extracellular acidification rate (ECAR) were recorded before and after serial injections of oligomycin and rotenone/antimycin A to yield final concentrations of 0.5 μM.

Flow cytometric analysis

LS174T-cont and Mieap-KD cells cultured under normal conditions were harvested by trypsin-EDTA treatment. After adding complete growth media to inactivate trypsin, cells were centrifuged, washed with PBS, and incubated with 5 μM 2',7'-dichlorofluorescein-diacetate (Sigma) for 20 min at 37°C. After being washed with PBS, cells were immediately analyzed with an EC800 flow cytometry analyzer (Sony) using the 488-nm line.

Quantification and statistical analysis

FRAP data quantification

Fluorescence recovery rates were calculated using cellSens Imaging Software (Olympus), in which the intensity initially acquired after bleaching was set to 0 and the pre-bleaching intensity was set to 1. The normalized average fluorescence recovery was plotted in JMP 14.2.0 (SAS).

Crista data quantification

For quantification of crista data, crista area and outlines of mitochondrial sections in TEM images were marked manually using Adobe Photoshop CC, where normal crista morphology was identified by the presence of lamellar structures with distinct OsO₄ staining. Aberrant crista-like structures that were not observed in mitochondria of WT were excluded. Subsequently, the ratio of crista area per mitochondrial section was calculated from the indicated number of mitochondria in legends of Fig. 8d, l, m, and 9f, using Image J⁷⁸.

Statistical analysis

Statistical analyses were performed in JMP 14.2.0 (SAS). Levels of significance in Figure 6i, 8a, 8b, 8d, 8h–j, 8l, 8n, 9b–d, 9f, S10b–d, S10f–h were assessed using Student’s two-tailed t-tests. Levels of significance in mass spectrometric analyses for biological replicate pairs shown in Figure 5a, 5b, 8e, and 8f were assessed using the paired two-tailed t-test. $p < 0.05$ was considered statistically significant. Asterisks were allotted to all the Figures containing statistical analyses as follows: *, $p < 0.05$; **, $p < 0.01$, ***, $p < 0.001$, ****, $p < 0.0001$.

Data visualization

Visualization of the experimental data subjected to statistical analyses were performed using Graph Builder engine in JMP 14.2.0 (SAS). When the data were visualized using violin plots, box plots were overlaid. The center line in the box indicates the median. The bottom and top of the box indicate the 25th and 75th percentiles. The whiskers extend 1.5 times the interquartile range (IQR) from the top and bottom of the box unless the minimum and maximum values are within the IQR. The values which fall above or below the whiskers are plotted individually as outliers.

Data availability

The datasets generated during the mass spectrometric analyses of cardiolipin are included in Supplementary Data 1, and available in the Metabolomics Workbench repository, [<https://www.metabolomicsworkbench.org/data/DRCCMetadata.php?Mode=Project&ProjectID=PR001192>], under Project ID PR001192. All other relevant data which support the findings of this study are included in this article and its supplementary information files. Source data are provided with this paper.

Code availability

The codes used for data analysis are available from the corresponding author upon a request.

Declarations

Acknowledgments

We thank H. Suzuki and M. Tsuneki for their contributions to *in vitro* and IHC experiments, respectively. This work was supported by grants from The National Cancer Center Research and Development Fund

(29-E-1, 30-A-3), JSPS KAKENHI Grant Numbers JP-19K07655, JP-19K07703, JP-17H06267 and JP-20K20305, and The Naito Foundation.

Author contributions

NI, YN, and HA performed *in vitro* experiments. KH, YS, and YN contributed to animal experiments. NI and HA analyzed data. NI and HA designed the research. NI and HA wrote paper. HA coordinated and supervised the project.

Declaration of interests

The authors declare no competing interests.

References

1. Shin, Y., and Brangwynne, C.P. Liquid phase condensation in cell physiology and disease. *Science* **357**, eaaf4382 (2017).
2. Boeynaems, S. et al. Protein Phase Separation: A New Phase in Cell Biology. *Trends Cell Biol.* **28**, 420–435 (2018).
3. Alberti, S., Gladfelter, A., and Mittag, T. Considerations and Challenges in Studying Liquid-Liquid Phase Separation and Biomolecular Condensates. *Cell* **176**, 419–434 (2019).
4. Sabari, B.R. et al. Coactivator condensation at super-enhancers links phase separation and gene control. *Science* **361**, eaar3958 (2018).
5. Case, L.B., Zhang, X., Ditlev, J.A., and Rosen, M.K. Stoichiometry controls activity of phase-separated clusters of actin signaling proteins. *Science* **363**, 1093–1097 (2019).
6. Huang, W.Y.C. et al. A molecular assembly phase transition and kinetic proofreading modulate Ras activation by SOS. *Science* **363**, 1098–1103 (2019).

7. Du, M.J., and Chen, Z.J.J. DNA-induced liquid phase condensation of cGAS activates innate immune signaling. *Science* **361**, 704–709 (2018).
8. Woodruff, J.B. et al. The centrosome is a selective condensate that nucleates microtubules by concentrating tubulin. *Cell* **169**, 1066–1077 (2017).
9. Rai, A.K., Chen, J.X., Selbach, M., and Pelkmans, L. Kinase-controlled phase transition of membraneless organelles in mitosis. *Nature* **559**, 211–216 (2018).
10. Welch, G.R. On the role of organized multienzyme systems in cellular metabolism: a general synthesis. *In Prog. Biophys. Mol. Biol.* (London, UK: Elsevier), pp. 103–191 (1977).
11. Sreere, P.A. Complexes of sequential metabolic enzymes. *Annu. Rev. Biochem.* **56**, 89–124 (1987).
12. Jin, M.Y. et al. Glycolytic Enzymes Coalesce in G Bodies under Hypoxic Stress. *Cell Rep.* **20**, 895–908 (2017).
13. Lee, H., DeLoache, W.C., and Dueber, J.E. Spatial organization of enzymes for metabolic engineering. *Metab. Eng.* **14**, 242–251 (2012).
14. Kohnhorst, C.L. et al. Identification of a multienzyme complex for glucose metabolism in living cells. *J. Biol. Chem.* **292**, 9191–9203 (2017).
15. Schmitt, D.L., and An, S. Spatial Organization of Metabolic Enzyme Complexes in Cells. *Biochemistry* **56**, 3184–3196 (2017).

16. An, S.G., Kumar, R., Sheets, E.D., and Benkovic, S.J. Reversible compartmentalization of de novo purine biosynthetic complexes in living cells. *Science* **320**, 103–106 (2008).
17. Kim, T.H. et al. Phospho-dependent phase separation of FMRP and CAPRIN1 recapitulates regulation of translation and deadenylation. *Science* **365**, 825-829 (2019).
18. Peeples, W. and Rosen, M.K. Mechanistic dissection of increased enzymatic rate in a phase-separated compartment. *Nat. Chem. Biol.* **17**, 693–702 (2021).
19. Macfarlane, M.G. Structure of cardiolipin. *Nature* **182**, 946 (1958).
20. Ikon, N., and Ryan, R.O. Cardiolipin and mitochondrial cristae organization. *Biochim. Biophys. Acta (BBA)-Biomembranes* **1859**, 1156–1163 (2017).
21. Paradies, G., Paradies, V., De Benedictis, V., Ruggiero, F.M., and Petrosillo, G. Functional role of cardiolipin in mitochondrial bioenergetics. *Biochim. Biophys. Acta (BBA)-Bioenergetics* **1837**, 408–417 (2014).
22. Ren, M.D., Phoon, C.K.L., and Schlame, M. Metabolism and function of mitochondrial cardiolipin. *Prog. Lipid Res.* **55**, 1–16 (2014).
23. Potting, C. et al. TRIAP1/PRELI complexes prevent apoptosis by mediating intramitochondrial transport of phosphatidic acid. *Cell Metab.* **18**, 287–295 (2013).
24. Ye, C., Shen, Z., and Greenberg, M.L. Cardiolipin remodeling: a regulatory hub for modulating cardiolipin metabolism and function. *J. Bioenerg. Biomembr.* **48**, 113–123 (2016).

25. Paradies, G., Paradies, V., Ruggiero, F.M., and Petrosillo, G. Role of cardiolipin in mitochondrial function and dynamics in health and disease: Molecular and pharmacological aspects. *Cells* **8**, 728 (2019).
26. Saric, A., Andreau, K., Armand, A.S., Moller, I.M., and Petit, P.X. Barth syndrome: from mitochondrial dysfunctions associated with aberrant production of reactive oxygen species to pluripotent stem cell studies. *Front Genet.* **6**, 359 (2016).
27. Acehan, D., Xu, Y., Stokes, D.L. and Schlame, M. Comparison of lymphoblast mitochondria from normal subjects and patients with Barth syndrome using electron microscopic tomography. *Lab Invest.* **87**, 40-48 (2006).
28. Dudek, J. et al. Cardiolipin deficiency affects respiratory chain function and organization in an induced pluripotent stem cell model of Barth syndrome. *Stem Cell Res.* **11**, 806-819 (2013).
29. Miyamoto, Y. et al. Possible Existence of Lysosome-Like Organelle within Mitochondria and Its Role in Mitochondrial Quality Control. *PLoS One* **6**, e16054 (2011).
30. Kamino, H. et al. Mieap-regulated mitochondrial quality control is frequently inactivated in human colorectal cancer. *Oncogenesis* **5**, e181 (2016).
31. Okuyama, K. et al. Mieap-induced accumulation of lysosomes within mitochondria (MALM) regulates gastric cancer cell invasion under hypoxia by suppressing reactive oxygen species accumulation. *Sci. Rep.* **9**, 2822 (2019).
32. Tsuneki, M., Nakamura, Y., Kinjo, T., Nakanishi, R., and Arakawa, H. Mieap suppresses murine intestinal tumor via its mitochondrial quality control. *Sci. Rep.* **5**, 12472 (2015).

33. Mussazhanova, Z. et al. Causative role for defective expression of mitochondria-eating protein in accumulation of mitochondria in thyroid oncocytic cell tumors. *Cancer Sci.* **111**, 2814–2823 (2020).
34. Gaowa, S. et al. Possible role of p53/Mieap-regulated mitochondrial quality control as a tumor suppressor in human breast cancer. *Cancer Sci.* **109**, 3910–3920 (2018).
35. Kitamura, N. et al. Mieap, a p53-Inducible Protein, Controls Mitochondrial Quality by Repairing or Eliminating Unhealthy Mitochondria. *PLoS One* **6**, e16060 (2011).
36. Feric, M. et al. Self-assembly of multi-component mitochondrial nucleoids via phase separation. *EMBO J.* **40**, e107165 (2021).
37. Kriventseva, E.V. et al. OrthoDB v10: sampling the diversity of animal, plant, fungal, protist, bacterial and viral genomes for evolutionary and functional annotations of orthologs. *Nucleic Acids Res.* **47**, D807–D811 (2019).
38. Huang, Y.J., Acton, T.B., and Montelione, G.T. DisMeta: a meta server for construct design and optimization. *Methods Mol. Biol.* **1091**, 3–16 (2014).
39. Uversky, V.N., Radivojac, P., Iakoucheva, L.M., Obradovic, Z., and Dunker, A.K. Prediction of intrinsic disorder and its use in functional proteomics. *Methods Mol. Biol.* **408**, 69–92 (2007).
40. Lupas, A., Van Dyke, M., and Stock, J. Predicting coiled coils from protein sequences. *Science* **252**, 1162–1164 (1991).
41. Holehouse, A.S., Das, R.K., Ahad, J.N., Richardson, M.O., and Pappu, R.V. CIDER: Resources to Analyze Sequence-Ensemble Relationships of Intrinsically Disordered Proteins. *Biophys. J.* **112**, 16–21 (2017).

42. Kyte, J., and Doolittle, R.F. A simple method for displaying the hydropathic character of a protein. *J. Mol. Biol.* **157**, 105–132 (1982).
43. Zarin, T. et al. Proteome-wide signatures of function in highly diverged intrinsically disordered regions. *Elife*. **8**, e46883 (2019).
44. Kaewsuya, P., Danielson, N.D., and Ekhterae, D. Fluorescent determination of cardiolipin using 10-N-nonyl acridine orange. *Anal. Bioanal. Chem.* **387**, 2775–2782 (2007).
45. Sathappa, M. and Alder, N.N. The ionization properties of cardiolipin and its variants in model bilayers. *Biochim. Biophys. Acta.* **1858**, 1362-1372 (2016).
46. Belazi, D., Sole-Domenech, S., Johansson, B., Schalling, M., and Sjoval, P. Chemical analysis of osmium tetroxide staining in adipose tissue using imaging ToF-SIMS. *Histochem. Cell Biol.* **132**, 105–115 (2009).
47. Planas-Iglesias, J. et al. Cardiolipin Interactions with Proteins. *Biophys. J.* **109**, 1282–1294 (2015).
48. Miyamoto, T. et al. Identification of 14-3-3 γ as a MIEAP-interacting protein and its role in mitochondrial quality control. *Sci. Rep.* **2**, 379 (2012).
49. Munnik, T., and Wierchowicka, M. Lipid-binding analysis using a fat blot assay. *Methods Mol. Biol.* **1009**, 253–259 (2013).
50. Bota, D.A., and Davies, K.J. Lon protease preferentially degrades oxidized mitochondrial aconitase by an ATP-stimulated mechanism. *Nat. Cell Biol.* **4**, 674–680 (2002).

51. Choi, S.Y. et al. A common lipid links Mfn-mediated mitochondrial fusion and SNARE-regulated exocytosis. *Nat. Cell Biol.* **8**, 1255–1262 (2006).
52. Banani, S.F. et al. Compositional Control of Phase-Separated Cellular Bodies. *Cell.* **166**, 651–663 (2016).
53. Lee, J.H. et al. The role of adipose tissue mitochondria: Regulation of mitochondrial function for the treatment of metabolic diseases. *Int. J. Mol. Sci.* **20**, 4924 (2019).
54. Sidossis, L. and Kajimura S. Brown and beige fat in humans: thermogenic adipocytes that control energy and glucose homeostasis. *J Clin Invest.* **125**, 478–486 (2015).
55. Fenzl, A. and Kiefer, F.W. Brown adipose tissue and thermogenesis. *Horm Mol Biol Clin Investig.* **19**, 25–37 (2014).
56. Crichton, P.G., Lee, Y., and Kunji, E.R. The molecular features of uncoupling protein 1 support a conventional mitochondrial carrier-like mechanism. *Biochimie.* **134**, 35–50 (2017).
57. Castellana, M. et al. Enzyme clustering accelerates processing of intermediates through metabolic channeling. *Nat. Biotechnol.* **32**, 1011–1018 (2014).
58. Prouteau, M., and Loewith, R. Regulation of Cellular Metabolism through Phase Separation of Enzymes. *Biomolecules* **8**, 160 (2018).
59. Strulson, C.A., Molden, R.C., Keating, C.D., and Bevilacqua, P.C. RNA catalysis through compartmentalization. *Nat. Chem.* **4**, 941–946 (2012).

60. Bracha, D., Walls, M.T., and Brangwynne, C.P. Probing and engineering liquid-phase organelles. *Nat. Biotechnol.* **37**, 1435–1445 (2019).
61. Zhao, E.M. et al. Light-based control of metabolic flux through assembly of synthetic organelles. *Nat. Chem. Biol.* **15**, 589–597 (2019).
62. Hinzpeter, F., Gerland, U., and Tostevin, F. Optimal Compartmentalization Strategies for Metabolic Microcompartments. *Biophys. J.* **112**, 767–779 (2017).
63. Su, X. et al. Phase separation of signaling molecules promotes T cell receptor signaltransduction. *Science.* **352**, 595–599 (2016).
64. Kojima, T., and Takayama, S. Membraneless Compartmentalization Facilitates Enzymatic Cascade Reactions and Reduces Substrate Inhibition. *ACS Appl. Mater. Interfaces* **10**, 32782–32791 (2018).
65. Feric, M. et al. Coexisting liquid phases underlie nucleolar subcompartments. *Cell.* **165**, 1686–1697 (2016).
66. Dan, X. et al. DNA damage invokes mitophagy through a pathway involving Spata18. *Nucleic Acids Res.* **48**, 6611–6623 (2020).
67. Tatsuta, T. and Langer, T. Quality control of mitochondria: protection against neurodegeneration and aging. *EMBO J.* **27**, 306-314 (2008).
68. Oshima, H. et al. Carcinogenesis in mouse stomach by simultaneous activation of the Wnt signaling and prostaglandin E-2 pathway. *Gastroenterology* **131**, 1086–1095 (2006).

69. Serricchio, M., Vissa, A., Kim, P.K., Yip, C.M., and McQuibban, G.A. Cardiolipin synthesizing enzymes form a complex that interacts with cardiolipin-dependent membrane organizing proteins. *Biochim. Biophys. Acta-Mol. Cell Biol. Lipids* **1863**, 447–457 (2018).
70. Tsukada, T. et al. Enhanced proliferative potential in culture of cells from p53-deficient mice. *Oncogene*. **8**, 3313–3322 (1993).
71. Goldstein, J.C., Waterhouse, N.J., Juin, P., Evan, G.I., and Green, D.R. The coordinate release of cytochrome c during apoptosis is rapid, complete and kinetically invariant. *Nat. Cell Biol.* **2**, 156–162 (2000).
72. Nakamura, Y. et al. BNIP3 and NIX mediate Mieap-induced accumulation of lysosomal proteins within mitochondria. *PLoS One* **7**, e30767 (2012).
73. Oda, K. et al. p53AIP1, a potential mediator of p53-dependent apoptosis, and its regulation by Ser-46-phosphorylated p53. *Cell* **102**, 849–862 (2000).
74. Wilkins, M.R. et al. Protein identification and analysis tools in the ExPASy server. *Methods Mol. Biol.* **112**, 531–552 (1999).
75. Shindou, H. et al. Docosahexaenoic acid preserves visual function by maintaining correct disc morphology in retinal photoreceptor cells. *J. Biol. Chem.* **292**, 12054–12064 (2017).
76. Yamamoto, T. et al. Decrease in membrane phospholipids unsaturation correlates with myocardial diastolic dysfunction. *PLoS One* **13**, e0208396 (2018).
77. Bligh, E.G., and Dyer, W.J. A rapid method of total lipid extraction and purification. *Can. J. Biochem.* **37**, 911–917 (1959).

Figures

Figure 1

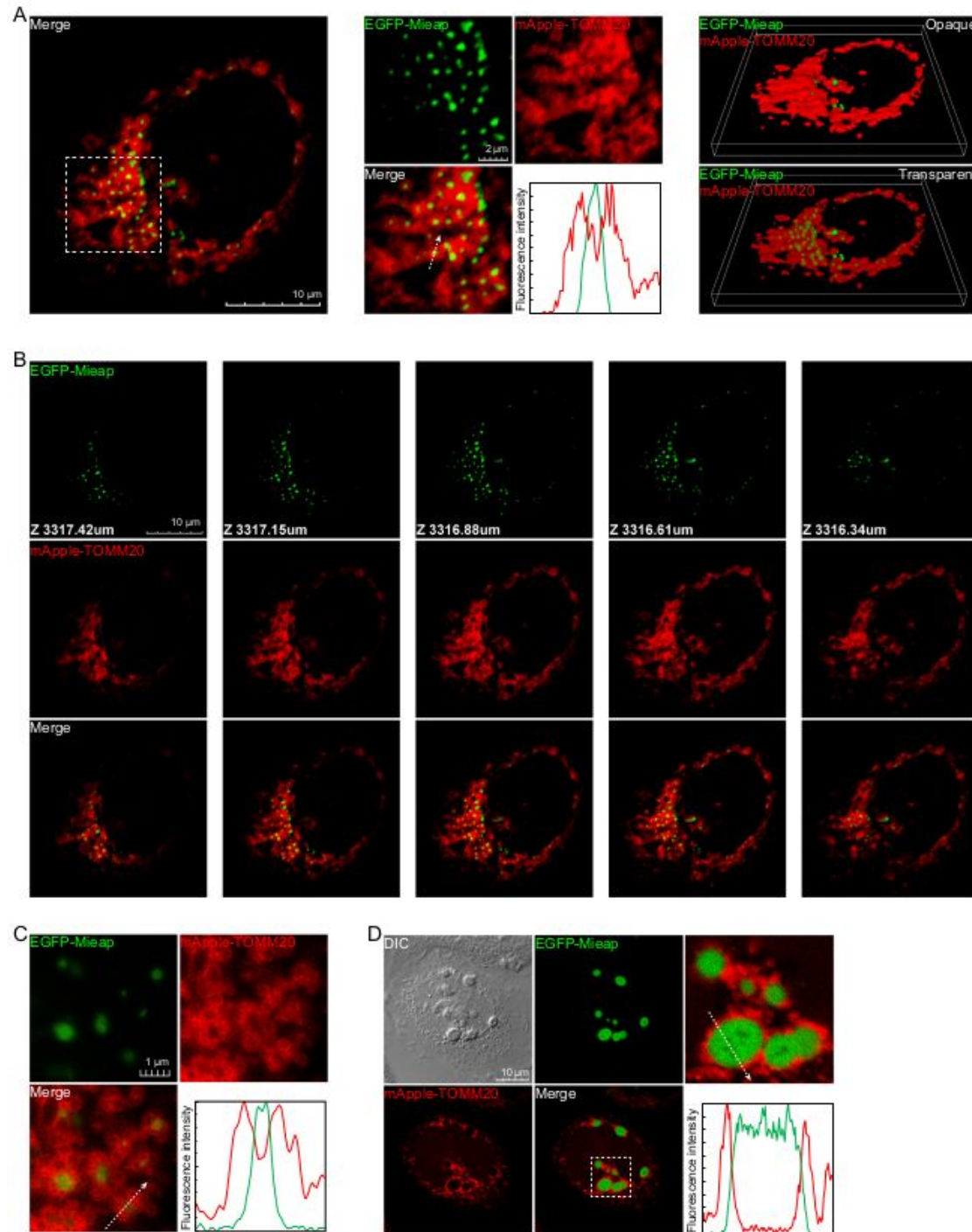


Figure 1

Mieap forms liquid droplets in mitochondria.

(a) Confocal microscopy showing the spatial relationship between Mi-BCs (EGFP-Mieap) and mitochondrial outer membranes visualized with mApple-TOMM20. Left: a cell image. Middle: higher magnification of the area indicated by the dashed square in the left panel and a line-scan of fluorescence intensities along the dashed arrow. Right: 3D reconstruction of the cell shown in the left panel. See also Supplementary Movie 3.

(b) Z-stack images of the cell in **(a)**.

(c) Super-resolution images showing the spatial relationship between Mi-BCs (EGFP-Mieap) and mitochondrial outer membranes, visualized with mApple-TOMM20.

(d) Confocal microscopy showing the spatial relationship between enlarged Mi-BCs and mApple-TOMM20. Lower right: line-scan as in **(a)**. See also Supplementary Movie 3.

Figure 2

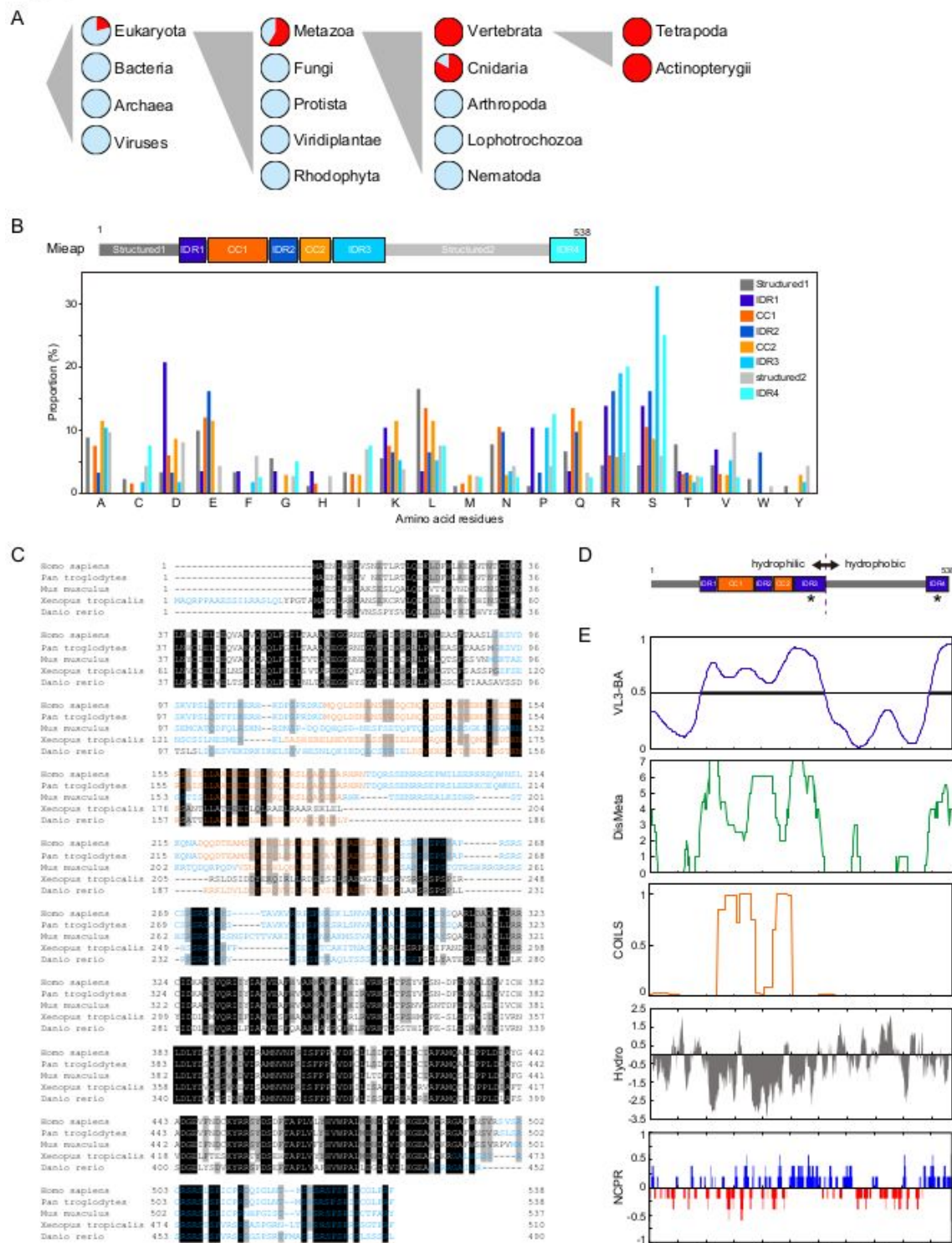


Figure 2

Mieap is an IDR-containing protein

(a) Phylogenetic spread of Mieap orthologs annotated with OrthoDB v10. Red sectors indicate present species. Light blue sectors indicate missing species.

(b) Proportion of amino acid residues in each domain of the Mieap protein.

(c) Multiple sequence alignment for Mieap orthologs in representative eukaryotes. Black and gray boxes indicate 100% and 80% identical residues among eukaryotes, respectively. Blue letters indicate IDRs annotated by VL3-BA. Orange letters indicate coiled-coil regions annotated by COILS.

(d) Schematic of the domain structure of Mieap. The dashed vertical line indicates the boundary of gross hydrophilic and hydrophobic halves, separated by IDR3 and the adjacent structured region. Asterisks indicate clusters of positively charged residues.

(e) Sequence analyses of Mieap protein. VL3-BA prediction of IDRs on the amino acid sequence of Mieap, in which bold lines indicate IDRs; DisMeta, meta-prediction of IDRs on the amino acid sequence of Mieap; COILS; coiled-coil regions annotated on the amino acid sequence of Mieap using a 21-residue sliding window; Hydro, hydrophobicity of Mieap using a 9-residue sliding window; NCPR, the linear net charge per residue of Mieap using a 5-residue sliding window.

Figure 3

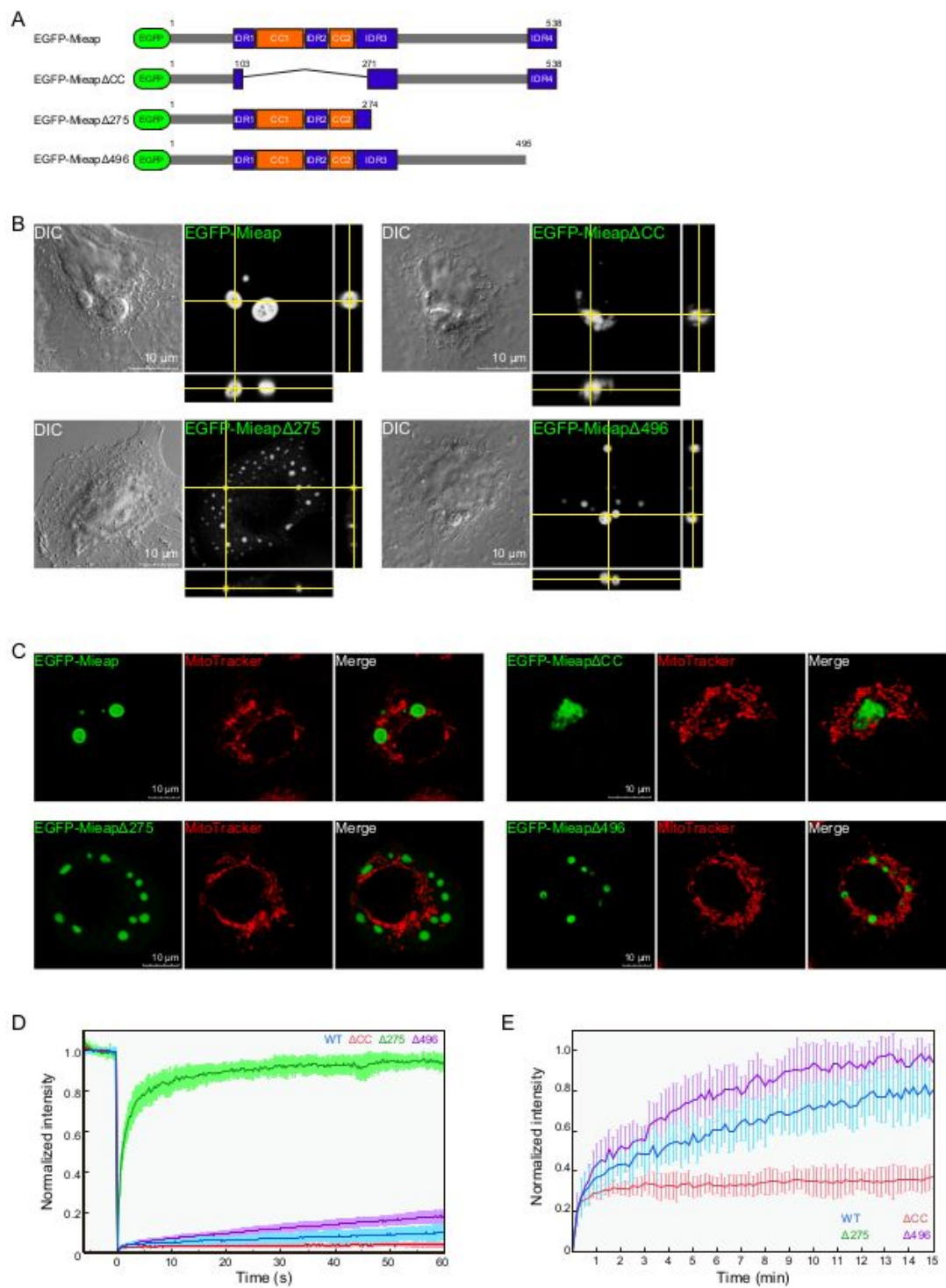


Figure 3

Material state and dynamics of Mi-BCs are determined by specific regions of Mieap.

(a) EGFP-Mieap and the three deletion-mutant forms. The schematic indicates wild-type (WT) and three deletion mutants (Δ CC, Δ 275, and Δ 496) of EGFP-Mieap protein. Numbers indicate amino acid residues.

(b) Representative images with a cross-sectional slice view of BCs formed by WT, Δ CC, Δ 275, and Δ 496 in A549 cells obtained with fluorescent confocal microscopy. See also Supplementary Movie 4.

(c) Subcellular localization of BCs formed by WT, Δ CC, Δ 275, and Δ 496, compared with a mitochondrial probe MitoTracker Red. See also Supplementary Movie 4.

(d) Normalized average fluorescence recovery in the FRAP experiment. Condensates formed by WT, Δ CC, Δ 275, and Δ 496 were analyzed in A549 cells. Each condensate was subjected to spot-bleaching using a 488-nm laser at 10% laser power with 11.6 μ s/ μ m exposure time and followed up for 60 s. n = 15 condensates for each construct. Data shown are means \pm SD.

(e) Normalized average fluorescence recovery in the FRAP experiment with weaker laser exposure as in **(d)**. Laser power was weakened to 1.4% and exposure time was shortened to 1.4 μ s/ μ m. Observation duration was expanded to 15 min after photobleaching entire condensates. n = 10 condensates for each construct. Data shown are means \pm SD.

Figure 4

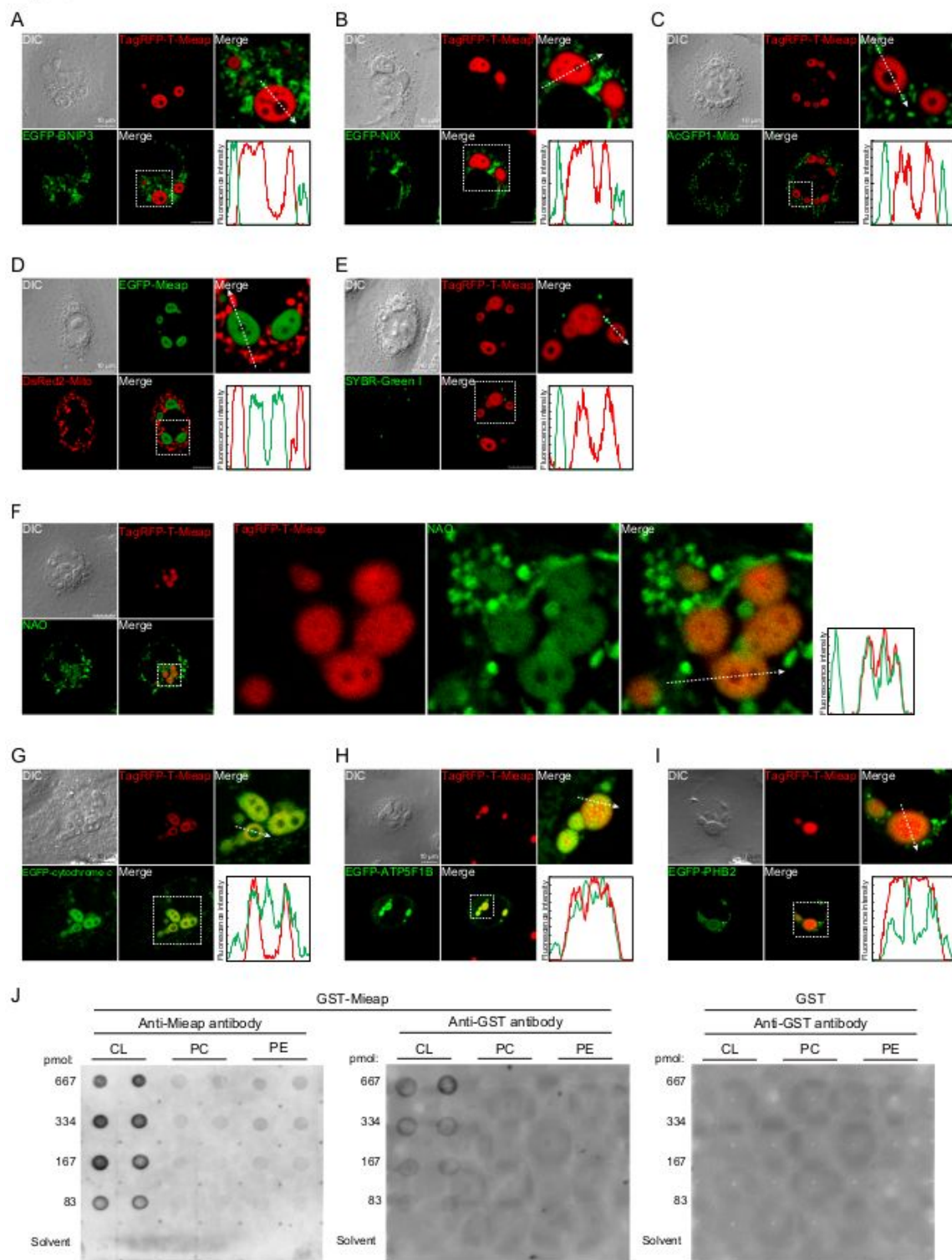


Figure 4

Mi-BCs phase-separate mitochondrial CL and CL-binding proteins.

(a – i) Live-cell imaging of Mi-BCs and various mitochondrial fluorescence probes in A549 cells. Whether each mitochondrial fluorescence probe is phase-separated by Mi-BCs was examined with live-cell imaging analysis in A549 cells. EGFP-BNIP3 (a), EGFP-NIX (b), AcGFP-mito (c), DsRed2-mito (d), and

SYBR Green I (**e**), were not incorporated into Mi-BCs. However, 10-nonylacridine orange bromide (NAO) (**f**), EGFP-cytochrome *c* (**g**), EGFP-ATP5F1B (**h**), and EGFP-PHB2 (**i**) were incorporated into Mi-BCs. Lower right: line-scan of fluorescence intensities along the dashed arrow. See also Supplementary Movies 5 and 6.

(j) Lipid-binding analysis of GST-tagged Mieap protein. GST-Mieap or GST was incubated with membranes on which increasing amounts of CL, phosphatidylcholine (PC), and phosphatidylethanolamine (PE), ranging from 0-667 pmol, were spotted. Protein-lipid interactions were visualized using an anti-Mieap antibody and/or anti-GST antibody, as indicated.

Figure 5

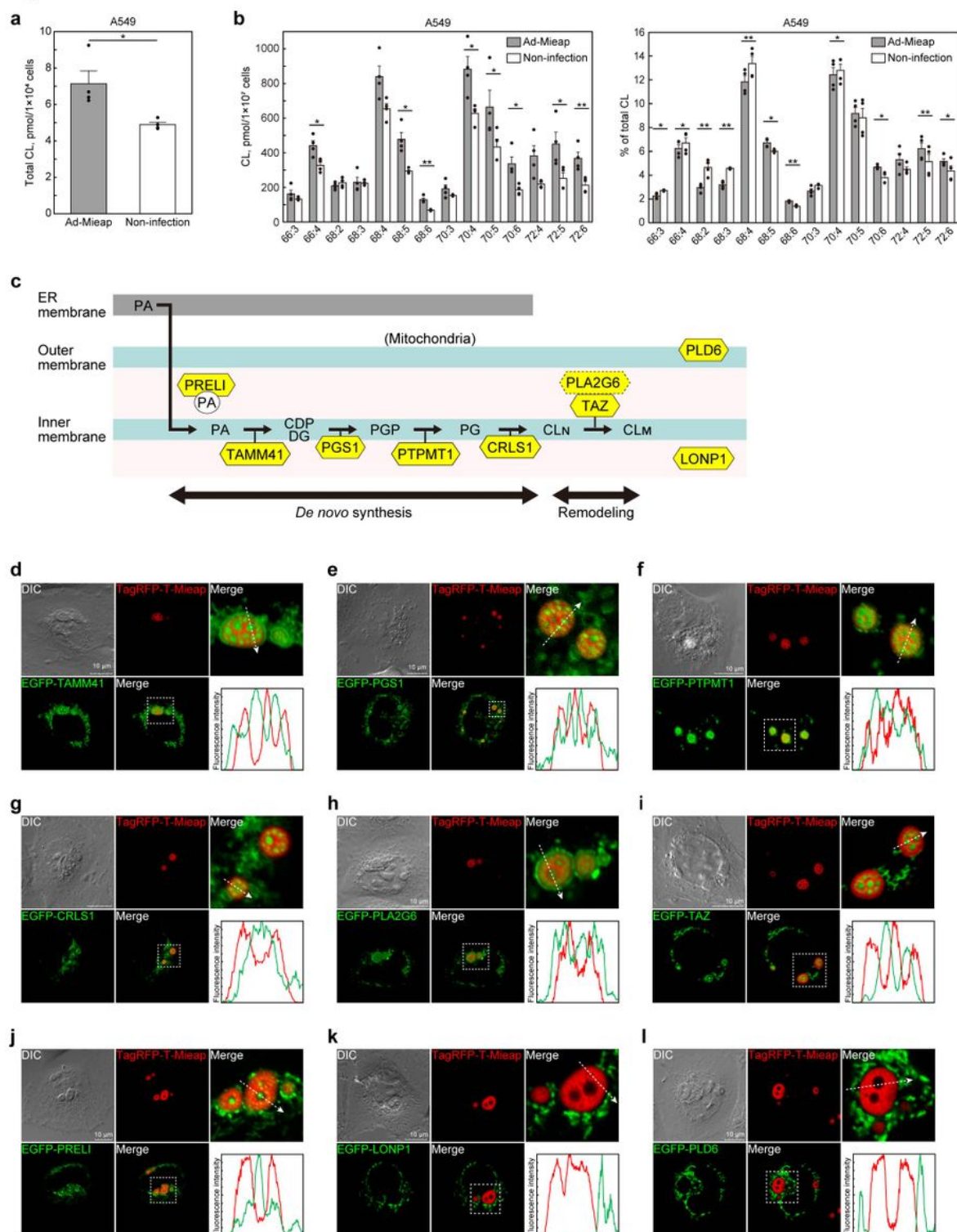


Figure 5

Mi-BCs compartmentalize and facilitate CL metabolic reactions.

(a) Quantitative assessment of total CL by mass spectrometric analysis. Uninfected A549 cells or cells infected with Ad-Mieap were subjected to mass spectrometric analysis for CL. Data shown are means \pm SE (n = 4). Statistical significance is indicated by * (p < 0.05).

(b) Quantitative and rate assessments of CL species by mass spectrometric analysis. A549 cells were analyzed as described in **(a)**. Absolute values of selected CL species are shown as amounts of substance per cell (left panel). Relative values of selected CL species are shown as % of total CL (right panel). Data shown are means \pm SE (n = 4). Statistical significance is indicated by * (p < 0.05), or ** (p < 0.01).

(c) The conventional CL metabolic pathway. Abbreviations: PA, phosphatidic acid; CDP-DG: cytidine diphosphate diacylglycerol; PGP, phosphatidylglycerophosphate; PG, phosphatidylglycerol; CL_N, nascent cardiolipin; CL_M, mature cardiolipin.

(d – j) Live-cell imaging of Mi-BCs and CL metabolic enzymes. EGFP-TAMM41 **(d)**, EGFP-PGS1 **(e)**, EGFP-PTPMT1 **(f)**, EGFP-CRLS1 **(g)**, EGFP-PLA2G6 **(h)**, EGFP-TAZ **(i)**, and EGFP-PRELI **(j)** were incorporated into Mi-BCs. Lower right: line-scan of fluorescence intensities along the dashed arrow. See also Supplementary Movie 7.

(k, l) Live-cell imaging of Mi-BCs and LONP1/PLD6. EGFP-LONP1 **(k)** and EGFP-PLD6 **(l)** were not incorporated into Mi-BCs. Lower right: line-scan of fluorescence intensities along the dashed arrow. See also Supplementary Movie 7.

Figure 6

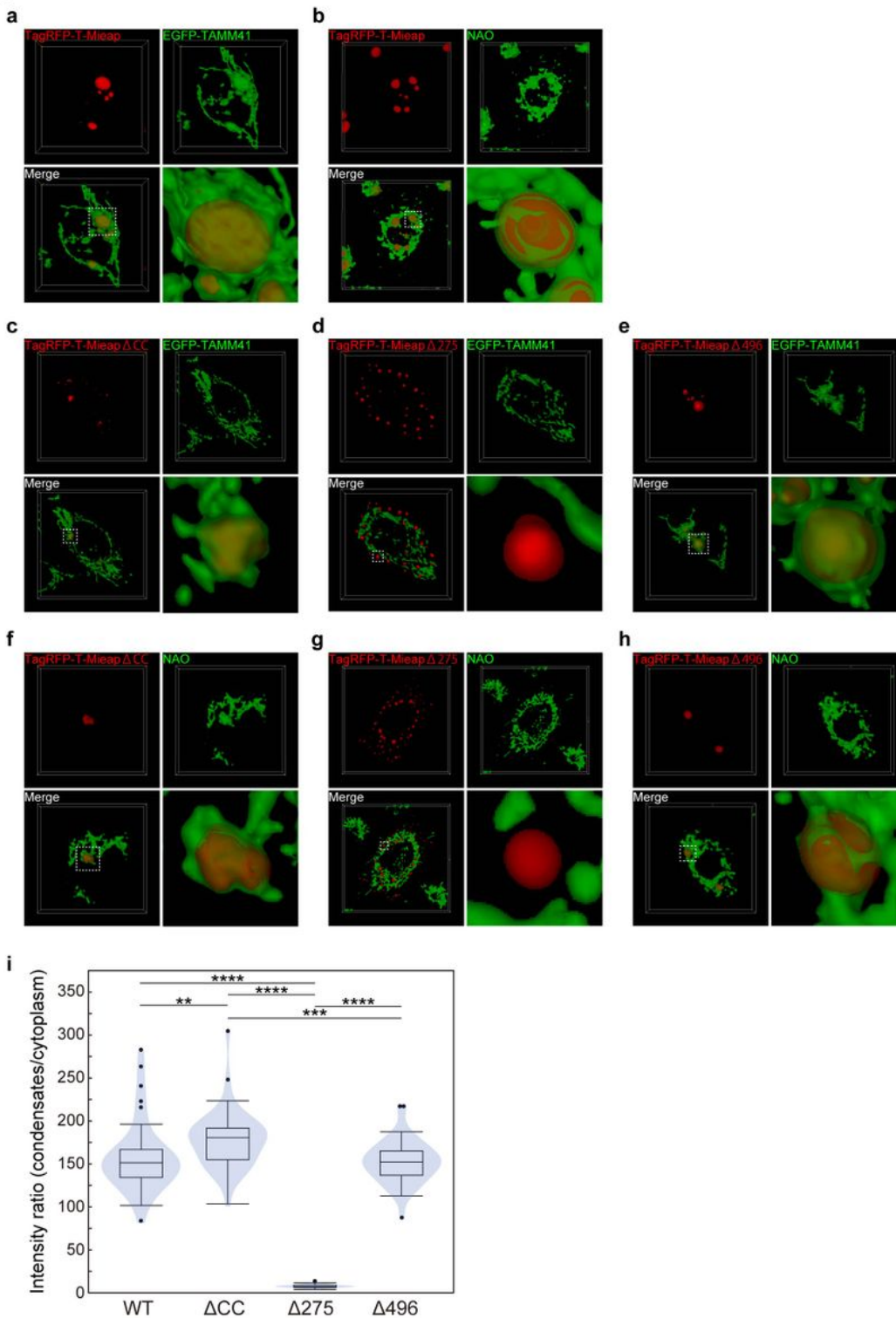


Figure 6

Mieap is highly concentrated in mitochondrial BCs.

(a) 3D reconstruction showing the spatial relationship between Mi-BCs (TagRFP-T-Mieap) and mitochondrial inner membranes visualized with EGFP-TAMM41 in HeLa cells. See also Supplementary Movies 8 and 10.

(b) 3D reconstruction showing the spatial relationship between Mi-BCs (TagRFP-T-Mieap) and NAO in A549 cells. See also Supplementary Movies 9 and 10.

(c – e) 3D reconstruction showing the spatial relationship between BCs formed by TagRFP-T-Mieap Δ CC **(c)**, Δ 275 **(d)**, and Δ 496 **(e)** and mitochondrial inner membranes visualized with EGFP-TAMM41 in HeLa cells. See also Supplementary Movies 8 and 10.

(f – h) 3D reconstruction showing the spatial relationship between BCs formed by TagRFP-T-Mieap Δ CC **(f)**, Δ 275 **(g)**, and Δ 496 **(h)** and NAO in A549 cells. See also Supplementary Movies 9 and 10.

(i) The intensity ratio (IR) of EGFP-Mieap WT, Δ CC, Δ 275, or Δ 496 protein in condensates and cytoplasm, displayed in violin plot. $n = 40$ cells for each construct in A549 cells. Statistical significance is indicated by ** ($p < 0.01$), *** ($p < 0.001$), or **** ($p < 0.0001$). When the data were visualized using violin plots, box plots were overlaid. The center line in the box indicates the median. The bottom and top of the box indicate the 25th and 75th percentiles. The whiskers extend 1.5 times the interquartile range (IQR) from the top and bottom of the box unless the minimum and maximum values are within the IQR. The values which fall above or below the whiskers are plotted individually as outliers.

Figure 7

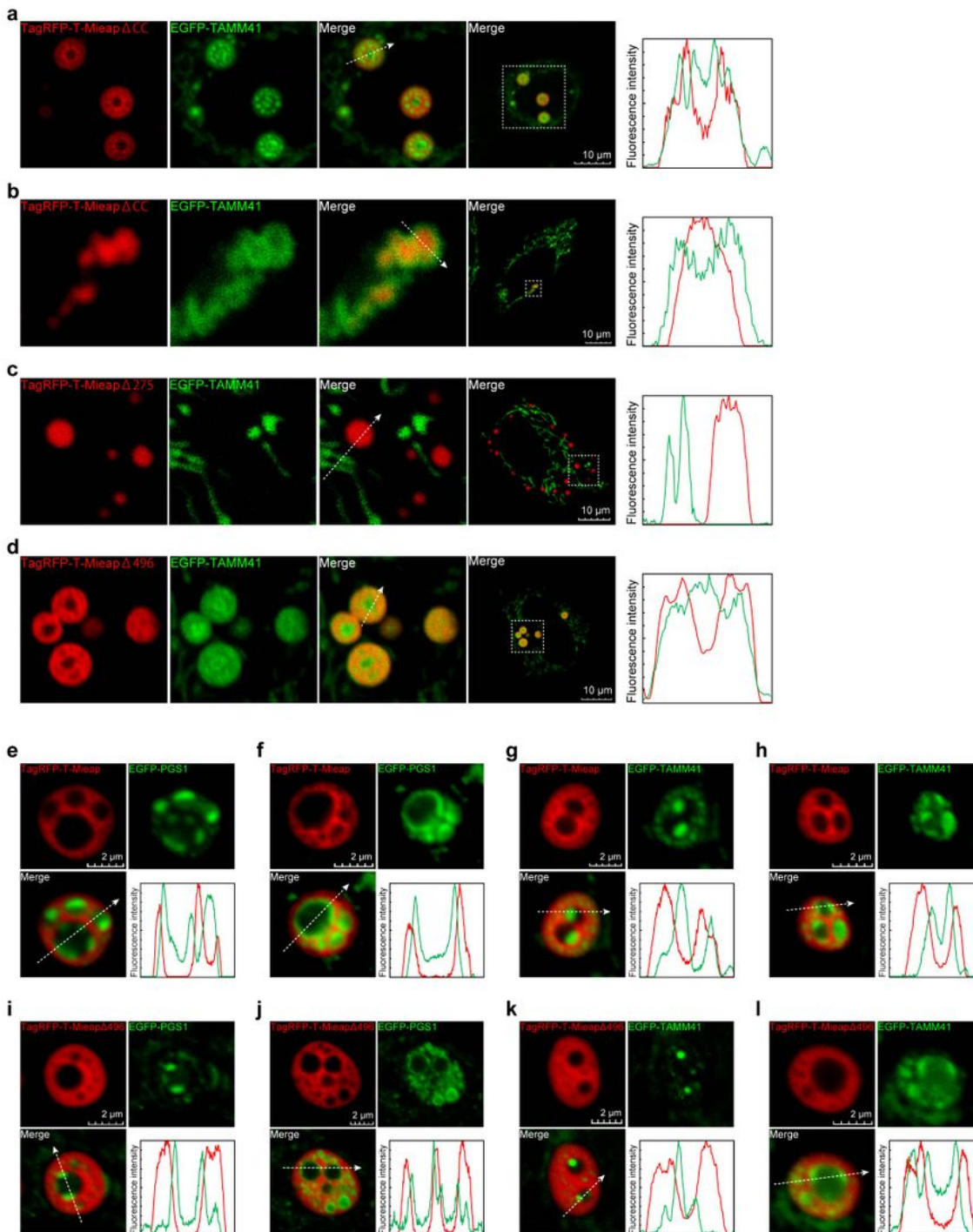


Figure 7

Both N- and C-terminal regions of Mieap are required to phase separate CL metabolic enzymes by generating the multi-phase structure of Mi-BCs.

(a – d) Comparison of phase-separating behaviors on the CL metabolic enzyme, TAMM41 (EGFP-TAMM41), between BCs formed by TagRFP-T-Mieap WT (a), Δ CC (b), Δ 275 (c), and Δ 496 (d) in HeLa

cells. Right: line-scan of fluorescence intensities along the dashed arrow.

(e – h) CL metabolic enzymes wet the interface in the Mieap-depleted phase of Mi-BCs. Distributions of the CL metabolic enzymes, EGFP-PGS1 (**e, f**) and EGFP-TAMM41 (**g, h**), in the Mieap-depleted phase of Mi-BCs are shown in HeLa cells. Lower right: line-scan of fluorescence intensities along the dashed arrow.

(i – l) CL metabolic enzymes wet the interface in the Mieap Δ 496-depleted phase of Δ 496-BCs. Distributions of the CL metabolic enzymes, EGFP-PGS1 (**i, j**) and EGFP-TAMM41 (**k, l**), in the Mieap Δ 496-depleted phase of BCs formed by the Δ 496 mutant are shown in HeLa cells. Lower right: line-scan as in (**e – h**).

Figure 8

Mieap may promote mitochondrial quality control by regulating CL metabolism.

(a) Oxygen consumption rates (OCR) of LS174T-cont and Mieap-KD cells under normal conditions calculated with a flux analyzer. Data are shown as means \pm SD (n = 9).

(b) Mitochondrial ATP production rates of LS174T-cont and Mieap-KD cells under normal conditions calculated with a flux analyzer, using a Seahorse XF real-time ATP rate assay. Data are shown as means \pm SD (n = 9).

(c) Morphology of mitochondria of LS174T-cont and Mieap-KD cells with transmission electron microscopy (TEM).

(d) Ratio of crista area per mitochondrial section of LS174T-cont and Mieap-KD cells. Quantitative data were obtained from cont mitochondria (n=197) and Mieap-KD mitochondria (n= 329) in TEM images and displayed in a violin plot.

(e) Quantitative assessment of total CL by mass spectrometric analysis. LS174T cells with (Cont) and without (Mieap-KD) endogenous Mieap expression were subjected to mass spectrometric analysis. Data shown are means \pm SE (n = 6).

(f) Quantitative and rate assessments of CL species by mass spectrometric analysis. LS174T cells were analyzed as described in **(e)**. Absolute values of selected CL species are shown as the amount of substance per cell (left panel). Relative values of selected CL species are shown as % of total CL (right panel). Data shown are means \pm SE (n = 6). See also Supplementary Data 1.

(g) The kinetic profile of the OCR using the Seahorse XF Real-Time ATP rate assay in HCT116 cells infected with Ad-Mieap or Ad-empty.

(h – j) Quantitative assessment of OCR **(h)**, mitochondrial ATP production rates **(i)**, and total ATP production rates **(j)** of the HCT116 cells as in **(g)**. Data are shown as means \pm SD (n = 9).

(k) Morphology of kidney mitochondria of $Mieap^{+/+}$ and $Mieap^{-/-}$ mice with TEM.

(l) Ratios of crista area per mitochondrial section of $Mieap^{+/+}$ and $Mieap^{-/-}$ mouse kidneys. Quantitative data were obtained from $Mieap^{+/+}$ kidney mitochondria (n=190) and $Mieap^{-/-}$ kidney mitochondria (n=234) in TEM images and displayed in a violin plot.

(m) Morphology of liver mitochondria of $Mieap^{+/+}$ and $Mieap^{-/-}$ mice with TEM.

(n) Ratios of crista area per mitochondrial section of $Mieap^{+/+}$ and $Mieap^{-/-}$ mouse livers. Quantitative data were obtained from $Mieap^{+/+}$ liver mitochondria (n=146) and $Mieap^{-/-}$ liver mitochondria (n=134) in TEM images and displayed in a violin plot. **(a, b, d, e, f, h-j, l, n)** Statistical significance is indicated by * ($p < 0.05$), ** ($p < 0.01$), *** ($p < 0.001$) or **** ($p < 0.0001$). When the data were visualized using violin plots, box plots were overlaid. The center line in the box indicates the median. The bottom and top of the box indicate the 25th and 75th percentiles. The whiskers extend 1.5 times the interquartile range (IQR) from the top and bottom of the box unless the minimum and maximum values are within the IQR. The values which fall above or below the whiskers are plotted individually as outliers.

Figure 9

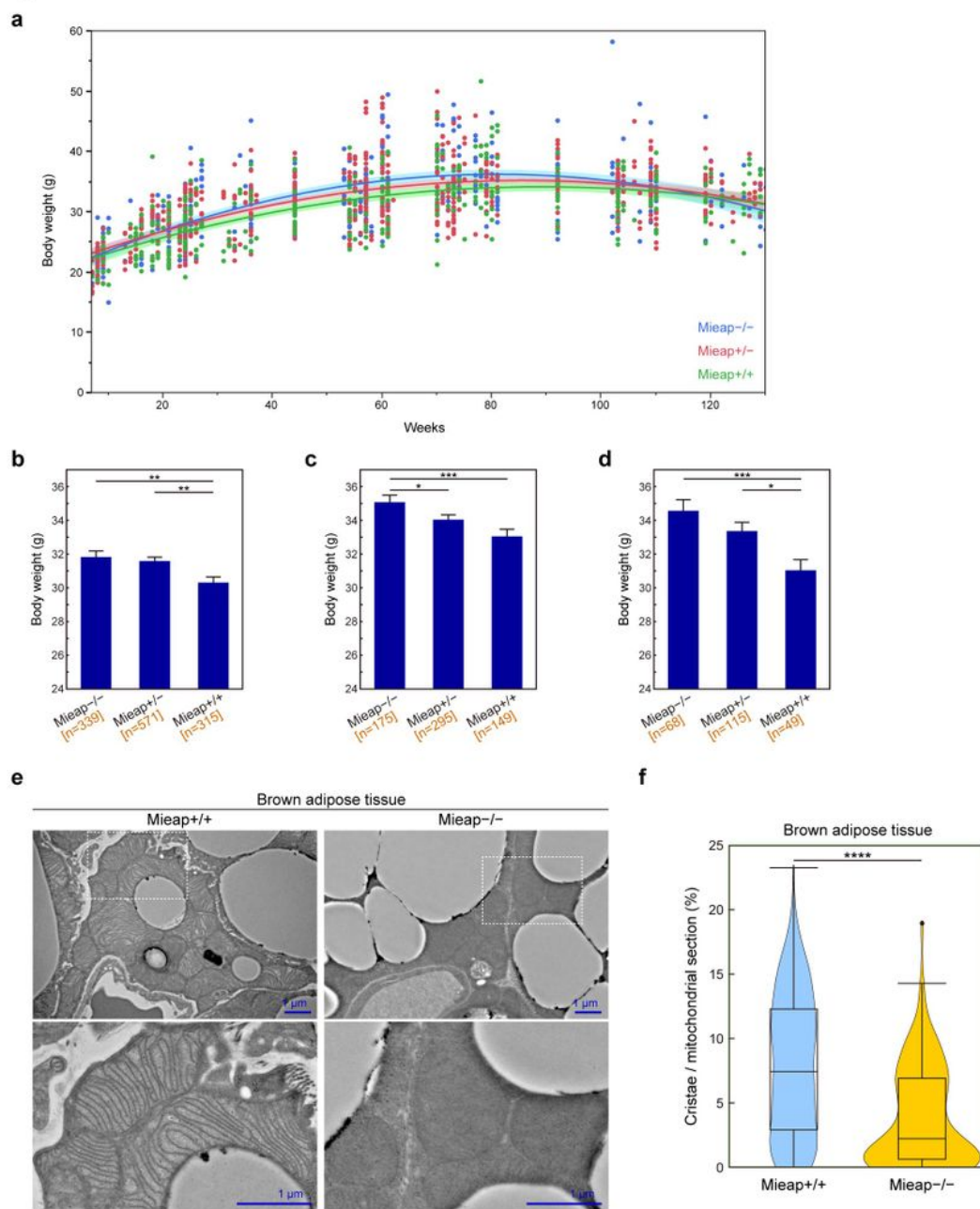


Figure 9

Mieap prevents obesity by regulating CL metabolism.

(a) Body weights of 1,225 Mieap^{+/+}, Mieap^{+/-}, and Mieap^{-/-} mice (n = 315 Mieap^{+/+}, 571 Mieap^{+/-}, and 339 Mieap^{-/-} mice, 7-130 weeks of age) were weighed. Dots and quadratic regression curves with 95% confidence intervals are shown for each genotype.

(b – d) Body weights of $Mieap^{+/+}$, $Mieap^{+/-}$, and $Mieap^{-/-}$ mice (7-130 weeks of age) **(b)**, (44-104 weeks of age) **(c)**, and (53-62 weeks of age) **(d)** in **(a)**. Data shown are means \pm SE. Statistical significance is indicated by * ($p < 0.05$), ** ($p < 0.01$), or *** ($p < 0.001$).

(e) Morphology of brown adipose tissue (BAT) mitochondria of $Mieap^{+/+}$ and $Mieap^{-/-}$ mice with TEM.

(f) The ratio of crista area per mitochondrial section of $Mieap^{+/+}$ and $Mieap^{-/-}$ mice BAT. Quantitative data were obtained from $Mieap^{+/+}$ BAT mitochondria ($n=181$) and $Mieap^{-/-}$ BAT mitochondria ($n=129$) in TEM images and displayed in a violin plot. Statistical significance is indicated by **** ($p < 0.0001$). The center line in the box indicates the median. When the data were visualized using violin plots, box plots were overlaid. The bottom and top of the box indicate the 25th and 75th percentiles. The whiskers extend 1.5 times the interquartile range (IQR) from the top and bottom of the box unless the minimum and maximum values are within the IQR. The values which fall above or below the whiskers are plotted individually as outliers.

Figure 10

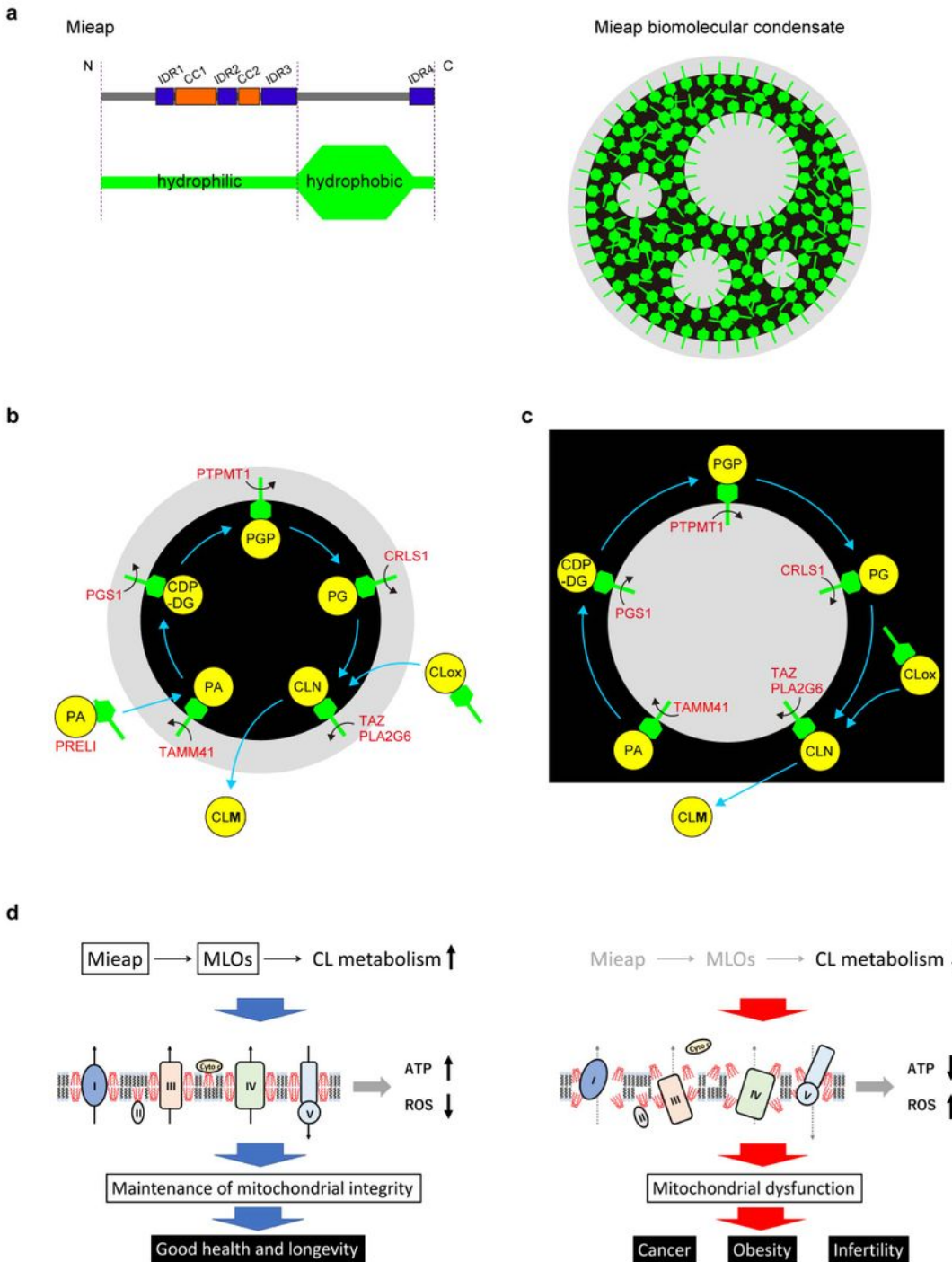


Figure 10

Hypothetical models for Mieap-mediated sequential enzymatic reactions in CL metabolism, which facilitates mitochondrial quality control.

(a) Hypothetical model of biosurfactant activity of Mieap. Mieap (green) exists in the Mieap-containing phase (lipid phase) (black), as a “scaffold” protein and/or as a potential “biosurfactant.” At the boundary

between the surfaces of Mi-BCs (aqueous phase) and the Mieap-containing phase (lipid phase) or between the Mieap-containing phase (lipid phase) and the Mieap-depleted phase (aqueous phase), the hydrophilic N-terminal end of Mieap always faces the aqueous phase at the boundary. **(b, c)** Hypothetical model for Mieap-mediated sequential enzymatic reactions in CL metabolism. Black areas indicate the Mieap-containing phase (lipid phase) containing CL and Mieap. Gray areas indicate the Mieap-depleted (aqueous phase) containing enzymes. Sequential reactions occur at the interface between the surface of Mi-BCs (aqueous phase) and the Mieap-containing phase (lipid phase) **(b)** or between the Mieap-containing phase (lipid phase) and the Mieap-containing phase (aqueous phase) **(c)**. Once Mieap (green) stably interacts with PA via its C-terminal region, one of the enzymes transiently and weakly interacts with the N-terminal region of Mieap. When Mieap interacts with TAMM41, PA is converted to CDP-DG. Such reactions between biosynthetic enzymes and corresponding substrates could be repeated until mature CL is produced. Concentration of enzymes and substrates at Mi-BC surfaces, segregation of enzymes and substrates into distinct sub-compartments of Mi-BCs, interfacial catalysis, and biosurfactant activity of Mieap may enable efficient sequential reactions for CL metabolism. Abbreviations: PA, phosphatidic acid; CDP-DG: cytidine diphosphate diacylglycerol; PGP, phosphatidylglycerophosphate; PG, phosphatidylglycerol; CLOX, oxidized cardiolipin; CLN, nascent cardiolipin; CLM, mature cardiolipin.

(d) A hypothetical model for mitochondrial quality control via the Mieap-MLOs-CL metabolism axis.

Supplementary Files

This is a list of supplementary files associated with this preprint. Click to download.

- [VideoS1light80X.mp4](#)
- [VideoS2light80X.mp4](#)
- [VideoS3light38sec.mp4](#)
- [VideoS4light38sec.mp4](#)
- [VideoS5light38sec.mp4](#)
- [VideoS6light80X.mp4](#)
- [VideoS7light38sec.mp4](#)
- [SupplementaryData1.xlsx](#)
- [SupplementaryData2.xlsx](#)
- [SupplementaryinformationIkarietal..pdf](#)
- [nrreportingsummaryIkarietal.pdf](#)
- [nreditorialpolicychecklist.pdf](#)
- [SupplementaryMovie8.mp4](#)
- [SupplementaryMovie9.mp4](#)
- [SupplementaryMovie10.mp4](#)